Inverse Scattering

of

Dielectric Cylinders

A Thesis Presented to

The Faculty of Graduate Studies

of

The University of Manitoba

In Partial Fulfillment of the

Requirements for the Degree of

Master of Science in Electrical Engineering

John Larrigan

October 1992

ISBN 0-315-77779-6

INVERSE SCATTERING OF DIELECTRIC CYLINDERS

BY

JOHN LARRIGAN

A Thesis submitted to the Faculty of Graduate Studies of the University of Manitoba in partial fulfillment of the requirements for the degree of

MASTER OF SCIENCE

I hereby declare that I am the sole author of this thesis.

I authorize the University of Manitoba to lend this thesis to other institutions or individuals for the purpose of scholarly research.

I further authorize the University of Manitoba to reproduce this thesis by photocopying or by other means, in total or in part, at the request of other institutions of individuals for the purpose of scholarly research.

Abstract

A two–dimensional microwave imaging algorithm based on inverse scattering is investigated. The algorithm uses the information contained in the scattered field to reconstruct the dielectric properties of an inhomogenious dielectric cylinder. The algorithm uses the method of moments to convert the integral equation, resulting from the solution of the Helmholtz equation, into a set of linear equations. Because of the nature of the problem, the resulting matrix equation is ill–conditioned. The matrix equation is solved to give a least square solution using a conjugate gradient method. The performance of the algorithm was evaluated by using a computer program to generate the dielectric cross section for a number of lossless and lossy target cylinders. Some of the results are shown as examples. A modified formulation is presented with the intention of improving performance of the algorithm when imaging cylinders are nearly symmetric.

ACKNOWLEDGEMENTS

The author wishes to thank Dr. L. Shafai for his patience and unquestionable support during the investigation of this thesis.

Table of Contents

List of Figures

Chapter 1 Introduction

Although microwave imaging is not as prominent as other imaging methods, it has its own unique advantages which makes it a promising investigative technique. In this thesis the characteristics of microwave imaging are further discussed, specifically the imaging of dielectric cylinders using an inverse scattering technique. Emphasis is placed on the imaging of lossy cylinders. Although this subject has the potential to have useful applications in many fields, most of the discussions are presented with medical applications in mind.

The advantages of microwave imaging give it a great potential in the areas of geological, industrial, and medical remote sensing. For geological studies, microwave imaging has been found to be useful in the detection of mineral deposits. In the industrial area, microwave imaging can be used for non–destructive testing of finished products. In the medical field, microwave imaging has taken a back seat to the more popular techniques such as X–ray computer aided tomography [CAT] and nuclear magnetic resonance [NMR] imaging. However, microwave imaging does have the potential to be a useful tool in the areas of microwave thermography and in some forms of diagnostic imaging. A through look at the medical applications of microwave imaging can be found in [1].

Microwave radiation has many inherent properties which can be used to detect objects. Materials are mathematically modeled with two parameters which describe the propagation of electromagnetic radiation within it. These are the dielectric constant ε_r and conductivity σ. Both of these properties are related to other physical properties such as temperature, electrolyte concentration, water content, and metal content to name a few. Changes in these

properties can produce a large enough contrast to show a detectable difference in the scattered field around an object. Using a microwave imaging technique, the changes in the dielectric constant and conductivity could be calculated, and this information can be used to calculate some of the corresponding properties previously listed. Another desirable characteristic, which could be beneficial to the medical field, is the ability of microwaves to penetrate air and bone. Ultrasound has a very high loss factor in air which makes it difficult to image some regions such as the lungs. X–rays on the other hand are only lossy in bone and show very little contrast in soft body tissue since the physical property that is used to generate an image is density. Although the effects of microwave radiation on biological beings are not totally understood, it is known that the ionization energy levels involved in performing a microwave image scan are far lower than the radiation levels involved with X–rays.

The major drawbacks to microwave imaging are the relatively long wavelength and nonlinear propagation of microwaves through inhomogenious dielectric mediums. However, when imaging objects with high dielectric constants, such as biological tissues, the wavelength is compressed by the dielectric, thereby, eliminating the problems associated with a long wavelength. In the case of X–rays, which travel in straight paths through objects, the imaging algorithms are easier to develop. Microwaves travel along nonlinear paths inside objects and create many internal reflections and refractions before exiting the target. These nonlinear propagation characteristics of microwave radiation give rise to extremely complicated imaging algorithms.

There are many types of microwave imaging systems and algorithms. Most early attempts at microwave imaging systems bore some resemblance to X–ray CAT scanners. Microwave imaging has since evolved into its own area of study, and now many different systems and algorithms have been developed. New algorithms have been developed which reconstruct the target object using the many different properties which exist in the scattered field, namely, (a) absorption, (b) reflection, (c) polarization, and (d) diffraction. The methods used to generate the dielectric composition also vary widely. Some methods are extensions of linear reconstruction algorithms taken from existing CAT scanning techniques, others borrow their theory from ultrasound reconstruction methods. The most promising and most difficult techniques are developed from electromagnetic theory. Most of these techniques utilize the method of moments [MOM] to change the integral equation which arises into a matrix equation. The solution of this matrix equation gives rise to another group of methods.

The case for using microwave imaging is a strong one. However, the techniques of today are still far from being developed to a point where they can be implemented effectively. As work in the area continues more accurate methods will be developed.

Chapter 2 Background Information

2. 1. Material Properties

The effects and properties of microwaves on materials are mathematically modeled using a number of parameters. These parameters and their symbols are dielectric permittivity ε, conductivity σ, and magnetic permeability μ. For the cases discussed in this thesis, the two properties which are of interest are the dielectric permittivity and conductivity. The magnetic properties are assumed to be known and constant. In the case of microwave imaging it is the spatial variation of the dielectric properties, both permittivity and conductivity, that are reconstructed using the scattered field produced from some type of interrogating field. A thorough look at the propagation of microwaves in biological tissue is covered in [2] and [3].

2. 2. Benefits and Applications

Microwave imaging possesses a number of benefits which makes it well suited for many applications. In addition, microwave imaging has some properties which makes it more suitable over existing imaging techniques for some applications. In the medical field, microwave scans can be accomplished by using relatively low ionization levels. Lin and Clarke [4] determined that the levels of energy required to penetrate biological targets to be less than 10 $\mu W/cm^2$. For imaging lungs, microwave imaging has an advantage over ultrasound imaging in its ability to penetrate bone and air. The most attractive property of microwave imaging is the large dielectric contrast among different biological tissues. In human soft tissue there is only a 2% diversity in X–ray absorption; whereas the dielectric

diversity of human soft tissue is very large. For example, the dielectric constant at microwave frequencies for fat is about 4 at the low end and is approximately 80 for cerebral spinal fluid at the high end [1]. Microwave imaging has the ability to extract some information which can be attributed to the dielectric constant of the target. Things such as the concentration of electrolytes in a solution have a great effect on the dielectric constant of fluids but have little or no effect on the X–ray absorption. In the case of NMR imaging, again, different information from the material under test is acquired since most NMR machines to date detect the concentration of hydrogen atoms in tissues.

For the purpose of diagnostic imaging, the dielectric constant of biological tissues can contain important information. As discussed earlier, the concentration of chemical ions in fluids has a great effect on the complex dielectric constant. This fact led researchers Jacobi and Larson to undertake extensive research in the area of imaging kidneys with microwave imaging [5] and [6]. In a kidney there are large ion concentration gradients between the different functioning areas. Knowing these concentration gradients and what effect certain treatments have on them would be of great benefit in the treatment of renal disorders. Figure 2.1 shows an example of a X–ray plate from a canine kidney, and figure 2.2 shows the corresponding microwave reconstruction of a kidney taken from [5].

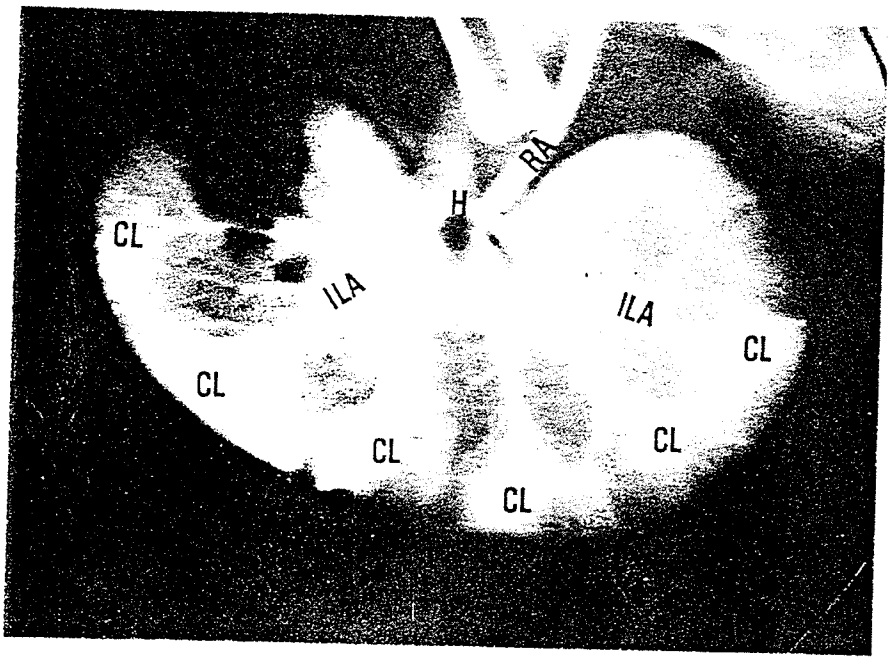

Fig. 2.1 – X-ray image of a canine kidney [5].

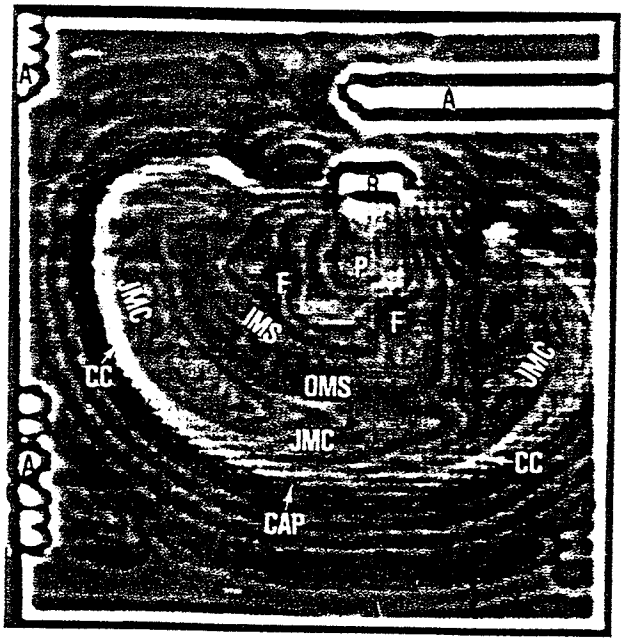

Fig. 2.2 – Microwave image of a canine kidney [5].

It is evident that the two images contain very different information. In the X–ray plate, the areas of higher density are more prominent. The most noticeable features are the renal arteries, interlobar arteries, and lobulations which are made up of a more dense tissue. In the case of the microwave reconstruction, the different layers of the kidney are more evident. This is primarily caused by the concentration gradients generated within the kidney as it filters blood. Blood to be filtered first enters the glomerulus which is located in the cortex (outer layer) of the kidney. As filtrate travels though the Loop of Henle, which transverses the kidney from the outer regions to the inner regions, the concentration of electrolyte in the filtrate is increased which leads to the large dielectric contrast between the regions.

Because the complex dielectric constant is largely proportional to water content, some researchers have used microwave imaging to detect forms of edema such as the study done by Iskander, Maini, Durney, and Bragg to measure pulmonary edema [7], and the work done by Lin and Clarke [4] in an attempte to image cerebral edema. Microwave imaging has some potential for observing pulmonary edema because microwaves can penetrate air easily. In the case of cerebral edema, the image quality may not be good enough for diagnostic purposes, but there is some potential use for monitoring the effects of treatments on a patient on a continuous basis where running a NMR image for a long period of time would not be practical and using X–rays would be dangerous.

Microwave hyperthermia is an experimental cancer treatment which uses microwave energy to kill malignant cancer cells. A review of microwave hyperthermia can be found in [8]. The treatment uses focused microwaves to heat the cancer cells to temperatures above

45^0 C where the cells die. However, it is important to limit the heating to the cancerous cell and to keep the heating of the surrounding healthy cells to a minimum. Many techniques are being studied which allow the microwave radiation to be focused inside biological bodies, but in order for the treatment to be fully effective, a thermographic map of the treated area should be known. Since there is a relation between temperature and dielectric constant of biological tissue, microwave imaging has the potential to generate a temperature profile of a treated area without affecting the treatment procedure [9][10].

2. 3. Liabilities and Remedies

Microwave imaging possesses some liabilities along with its benefits which have made the imaging technique unpopular for most applications. The most serious drawbacks in microwave imaging are the relatively long wavelength which reduces the resolution, external noise, and nonlinear propagation of the waves in the medium.

According to the Rayleigh criterion [11], and by the work done by Bolomey et al. [12] in the area of microwave diffraction imaging, objects must be in the order of $1/4\lambda$ to $1/2\lambda$ to be resolved. Since the wavelength of microwaves can be in the order of meters, this long wavelength can limit the resolution to a point where microwave imaging is no longer feasible. However, when imaging objects with a high dielectric constant, the problems associated with the wavelength are reduced since the wavelength in the object is proportional to $1/\sqrt{\epsilon_r}$. For medical applications it was determined by Lin [13] that the ideal frequencies for imaging of biological tissues ranged from 2.0 Ghz to 8.0 Ghz. This frequency range gives a range in wavelength of 15 cm to 3.75 cm in free space. In the case of human brain tissue,

which has a dielectric constant of around $\varepsilon_r = 30$ at microwave frequencies, a 15 cm wavelength would be reduced to 2.74 cm and a 3.75 cm wavelength would be reduced to 0.685 cm. This means that, theoretically, objects as small as 0.343 cm (half wavelength) could be resolved. If this resolution could be achieved in practice, then microwave imaging could become an effective investigative tool.

There is a trade off for using higher frequencies to get better resolution in some circumstances. Again, using the interrogation of biological tissue as an example, the loss in biological tissue is inversely proportional to the frequency. This consequently limits the depth to which the microwave energy can penetrate into the internal regions of a target and be recovered at a point outside of the object. This limits the ability to reconstruct areas which are situated deep inside an object.

Sampling the scattered field around a target is very susceptible to noise sources in the area. Some of the ways of getting around this problem are to increase the power of the interrogating field, average time sampling, and placing the system in an anechoic and noiseless environment. Increasing the interrogating power is a working option for non–living targets; however, since the full effect of electromagnetic radiation on humans is not totally known, this alternative is not considered acceptable. Average time sampling is a simple technique which assumes that the time average of noise is zero. Therefore, if the scattered field is sampled a number of times and then averaged, the average value of the noise should average out to zero leaving the true value for the field. The most common technique is to immerse the system into a water tank which serves three purposes. First, is to shield

the system from noise by attenuating the noise from exterior sources before they reach the receivers. Secondly, is to keep reflected signals of the incident field from corrupting the measurement data. Thirdly, the water provides a better impedance match between the antennas and the target. Jacobi, Larsen and Hast provide a look at the special considerations involved in designing antennas for under water use in microwave imaging in [14].

The most detrimental property which makes microwave imaging unpopular in almost all cases is the fact that microwaves do not travel in a straight line inside an inhomogenious dielectric object. Instead, they take numerous paths and refract and reflect off of dielectric boundaries. This makes imaging techniques significantly more complicated than techniques based on linear propagation such as X–rays. Some imaging techniques contained modifications to current X–ray linear reconstruction algorithms; whereas others utilized electromagnetic theory in order to reconstruct objects.

2. 4. Imaging Systems and Algorithms

In the last decade, many different types of imaging algorithms and systems have been developed. Although the algorithms used vary greatly, the systems used for measurements all fall into a relatively small number of categories. The most predominant of these categories are: transmission tomography, reflection tomography, and inverse scattering reconstruction. Transmission tomography is the same type of system used by early X–ray CAT scans [15]. The setup of the system is shown in figure 2.3 [16].

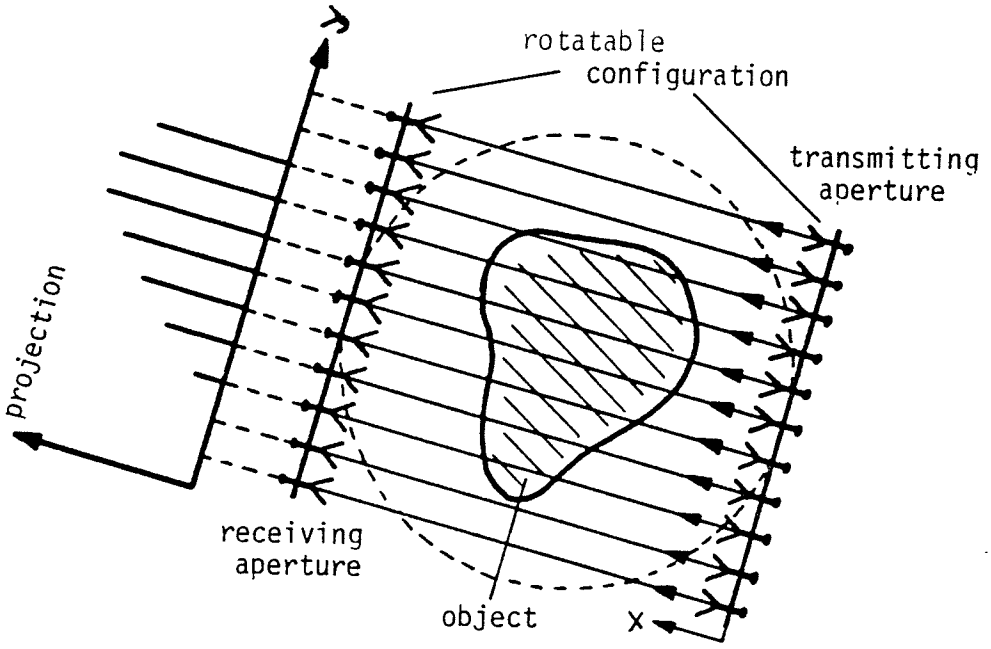

Fig. 2.3 – Transmission tomography system.

As shown, the setup consists of an array of transmitters and an opposing array of receivers. This type of setup is well suited for imaging throughout the entire target since the interrogating signal completely penetrates the object from one side to the other. However, for lossy targets the interrogating signal may be attenuated to such a degree that it may not be detectable at the receiving array. Reflection tomography has the transmitter and receiver at the same location and measures the reflected signals from discontinuities below the surface of the transmitter. This type of system is used in the geological field simply because it is impractical to place transmitters and receivers on the opposite side of the object. This technique is also favored when locating objects close to the surface of the target region since the scattered signal does not have to travel very far before it is detected. Finally, inverse scattering samples the scattered field around the object and then tries to reconstruct the dielectric profile using electromagnetic equations. In this thesis the imaging algorithm is based upon an inverse scattering technique.

In the field of microwave imaging, there are many parameters that can be used to reconstruct the original object. Some of these parameters are: absorption, phase, polarization, and reflection time. Typically some types of systems are better suited for recovering different parameters. In most cases the absorption is best measured using a transmission tomography type of system; whereas the reflected signals are best measured using a reflection tomography system.

Some attempts at microwave imaging have used linear reconstruction techniques borrowed from X–ray imaging algorithms. One method which was used was the arithmetic reconstructing technique [ART]. A study conducted [17] showed that ART was inadequate for use in microwave imaging and only simple objects could be reconstructed reliably. This approach and other linear reconstruction algorithms assumed that the microwave radiation propagates along a straight line. However, such assumptions were found to be too inaccurate. This led to various types of modifications on the existing linear reconstruction algorithms in an attempt to accommodate the nonlinear propagation of microwaves [18]. However, the resulting algorithms became too complicated to be of any practical use. One of the more successful attempts at using linear reconstruction techniques was done by Jacobi and Larsen using a technique based on linear FM pulse compression radar [19]. This technique used a pulse of FM microwave radiation and a receiver which only measured the signal during a certain time interval. The idea was that the signals which arrived at the receiver first had taken the shortest path which was assumed to be an almost linear path.

Other attempts at microwave imaging are based on inverse scattering. These methods used the scattered field produced by some interrogating field to reconstruct the dielectric properties of the target. These techniques are based upon solving the wave equation inside the target region. A large majority of these algorithms utilize the MOM to solve the wave equation numerically. The MOM transfers the integral equation solution of the wave equation into a set of linear equations [20]. The resulting matrix is ill–conditioned and the solution of it is the area of much research. In a paper by Ney, Smith, and Stuchly [21] the matrix is solved by using the pseudoinverse. Some other methods take an iterative approach. One method for solving the wave equation presented recently was based upon simulated annealing [22]. This method required a large number of iterations (25 000 as shown in one example) to converge to a result and in some cases may not converge at all. Another technique recently published applied the Newton Kantorovich procedure to reduce the number of iterations [23]. This method also is an iterative method but involves solving a matrix equation with each iteration which in the end will lead to large execution times.

In a recent paper by Caorse, Gragnani and Pastonino [24] a technique for calculating the cross section of a lossless dielectric cylinder was presented. This method was based on the MOM, and the ill–conditioned matrix resulting from the technique was solved by the pseudoinverse described in Ney [25]. The purpose of this work is to present the results of this technique using a conjugate gradient method to solve the ill–conditioned matrix and to present the results from a lossy cylinder.

Chapter 3 Computer Simulation

3. 1 Measurement Region Setup

The setup used to generate the scattered field measurements is shown below in figure 3.1.

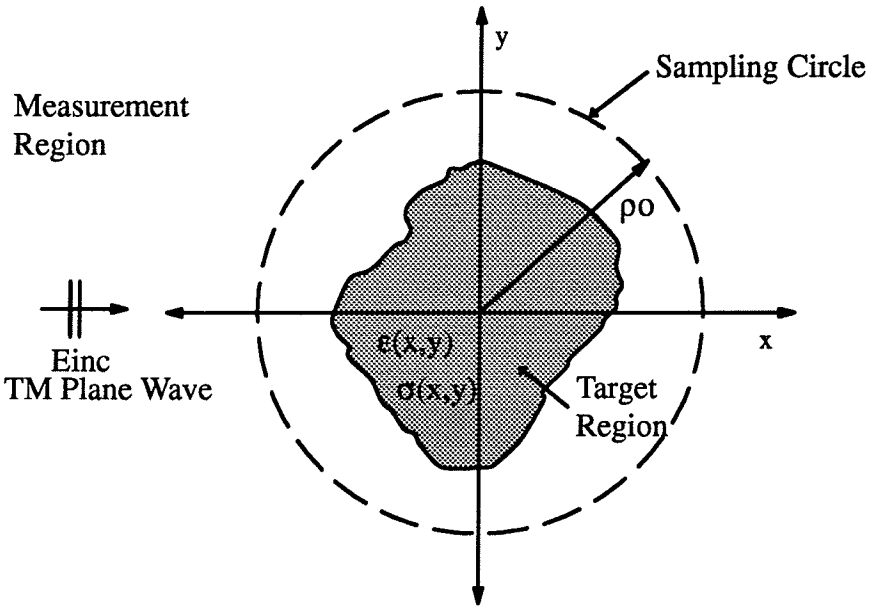

Fig. 3.1 – Setup of target within measurement region.

The target in the region is an infinite cylinder parallel with the *z* axis. The dielectric constant ε_r and conductivity σ are functions of *x* and *y* over the cross section of the cylinder. The magnetic permeability μ is constant over both the target and measurement regions and is equal to the free space permeability μ_o. The cylinder is illuminated with a transverse magnetic [TM] plane wave with the electric field parallel to the *z* axis and is incident from the negative *x* direction. The scattered field produced from the incident plane wave is sampled at evenly spaced points on a circle of radius ρ_o. In the measurement region outside

the cylinder, the dielectric permittivity is taken to be $\varepsilon_r = \varepsilon_o$, and the conductivity $\sigma = 0$. The scattered field is calculated at the sampling points using the well known Richmond technique [26].

To simplify the formulation and to make the values of ε_s and σ_s more manageable, the dielectric properties of the target region are described using the complex dielectric constant $\varepsilon_r = \varepsilon_r^*$, where ε_r^* is as follows:

$$\epsilon^*_r = \epsilon' - j\epsilon'' \tag{3.1}$$

and

$$\epsilon' = \epsilon_r \text{ and } \epsilon'' = \frac{\sigma}{\omega\epsilon_o} \tag{3.2}$$

where ω is the frequency in radians/s. Using this representation for the dielectric constant simplifies the formulation of the propagation constant. The propagation constant in the measurement region is

$$k_o = \sqrt{\omega^2 \mu_o \epsilon_o} \tag{3.3}$$

and the propagation constant in the measurement region is as follows:

$$k_s(x,y) = \sqrt{\omega^2 \mu_o \epsilon_s(x,y)} \tag{3.4}$$

3. 2 Formulation

The formulation investigated here is based upon solving the Helmholtz equation inside the target region and at selected points in the measurement region. Since the incident

field is parallel to the cylinder axis and the cylinder is infinite along the z axis, all of the electric fields will only have components along the z axis. This simplifies the problem by changing the vector Helmholtz equation to the following scalar one:

$$[\nabla^2 + k^2]\ \Psi(x,y) = 0 \tag{3.5}$$

where k is the propagation constant in either the measurement region (3.3) or in the target region (3.4) depending on what domain x and y are in. In the case of a scattered field produced by a current distribution J, the following Helmholtz equation must hold

$$[\nabla^2 + k^2]\ E_{scat}(x,y) = -j\omega\mu_o J \tag{3.6}$$

where E_{scat} is the scattered field and J is a current distribution which in this case is produced by an incident electric field upon a dielectric cylinder. In order to solve equation (3.6) the following similar problem is solved using the Green's function:

$$[\nabla^2 + k^2]\ G(k\varrho) = -\delta(k\varrho) \tag{3.7}$$

where G(k ρ) is the following two dimensional Greens's function

$$G(k\varrho) = \frac{j}{4} H_o^2(k\varrho) \tag{3.8}$$

and

$$\varrho = \sqrt{(x-x')^2 + (y-y')^2} \tag{3.9}$$

where x' and y' are points in the target region, x and y are the coordinates of the points where the scattered field is sampled, and H_o^2 is the zero order Hankel function of the second kind. Equation (3.8) represents the impulse response of equation (3.7). To get the entire solution one must superimpose all of the impulse responses by integrating over the domain of equation (3.7). However, to solve equation (3.6) the unit impulse responses are converted to current elements and then superimposed by integration. This gives the following solution for the scattered field:

$$E_{scat}(x,y) = \int_s -J_s(x,y)\ G(k_o\varrho)ds \tag{3.10}$$

To relate the current distribution to the physical parameters of the cylinder, the following relation is used:

$$J_s(x,y) = (j\omega\mu_o)^{-1}[k_s^2(x,y) - k_o^2]\ E_{tot}(x,y) \tag{3.11}$$

where J_s is the polarization current and E_{tot} is the total electric field.

The first step in reconstructing the dielectric profile of the object is to solve equation (3.10) for the polarization current J_s. After $J_s(x,y)$ is known it is then used along with the incident field to calculate the total electric field. Once both the polarization current and the total electric field are known, then equation (3.11) can be used to find the propagation constant $k_s(x,y)$ for the region, and it is then a simple matter of extracting the dielectric constant and conductivity from $k_s(x,y)$ using the relations described by equations (3.1) to (3.4).

The first step in solving equation (3.10) for the polarization current is to spatially discretize the domain of the unknown function $J_s(x,y)$. This is one of the techniques used by Richmond in [26]. This technique converts the function $J_s(x,y)$ into a summation of patches in the region which is shown mathematically as follows:

$$J_s(x,y) = \sum_m Js_m(x_m, y_m) \tag{3.12}$$

where m is the number of patches that J_s is discretized into. In this case the target region is taken as a square, and it is broken up into square patches with the same number of patches on each side. Figure 3.2 shows the spatial discretization of the target space used in this paper.

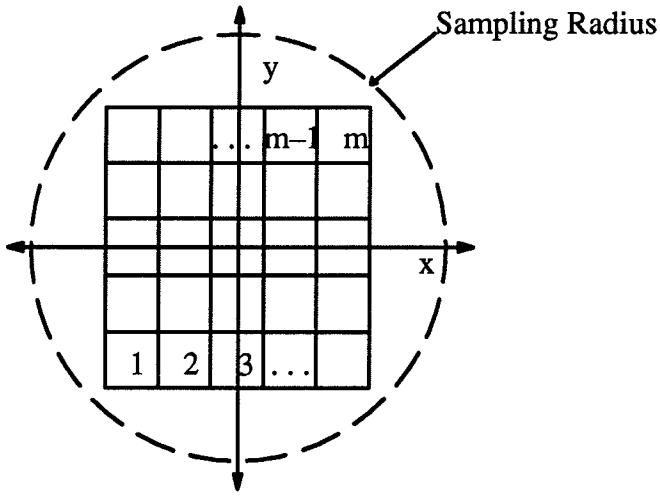

Fig. 3.2 – Discretization of target space.

Substituting (3.12) into equation (3.10) gives the following:

$$E_{scat}(x,y) = \int_s -\frac{j}{4}\sum_m Js_m(x'_m, y'_m)H_o^2(k_o\varrho)ds \tag{3.13}$$

Since values for x_m and y_m lie within the target region they become x_m' and y_m'. Multiplying both sides of equation (3.13) by a weighting function, in this case a delta function, and summing up over the domain of the left hand side gives:

$$\sum_n E_{scat_n}(x_n, y_n) = \sum_n \int_s -\frac{j}{4} \sum_m Js_m(x'_m, y'_m) H_o^2(k_o \varrho) ds \tag{3.14}$$

where n turns out to be the number of points where the scattered field is sampled. If the polarization current Js is assumed to be constant over each patch, then the summation of Js can be brought outside of the integral operation, giving the following:

$$\sum_n E_{scat_n}(x_n, y_n) = -\sum_n \sum_m Js_m(x'_m, y'_m) \frac{j}{4} \int_s H_o^2(k_o \varrho) ds \tag{3.15}$$

where ρ is now

$$\varrho = \sqrt{(x_n - x'_m)^2 + (y_n - y'_m)^2} \tag{3.16}$$

If the area of each patch is assumed to be a circle then the integration of the Hankel function can be evaluated to give the following result:

$$\frac{j}{4} \int_s H_o^2(k_o \varrho) ds = \frac{\pi a}{2k} J_1(ka) H_o^2(k_o \varrho) \tag{3.17}$$

where a is the radius of a circle with equal area of a patch in the target region, and J_1 is the first order Bessel function. Substituting equation (3.17) into (3.15) gives the following:

$$\sum_n E_{scat_n}(x_n, y_n) = -\sum_n \sum_m Js_m(x'_m, y'_m) \frac{j\pi a}{2k_o} H_o^2(k_o \varrho) ds \tag{3.18}$$

The above equation can now be rewritten in terms of a matrix equation. The matrix equation representation is as follows:

$$Es_{nx1} = [\mathbf{M}]_{mxn}\, Js_{mx1} \tag{3.19}$$

where

$$\mathbf{M}_{ij} = -\frac{j\pi a}{2k_o} J_1(k_o a) H_o^2(k_o \rho) \tag{3.20}$$

The resulting matrix [**M**] is ill–conditioned and must be solved using some special algorithm which can deal with it. In this case equation (3.19) was solved for the polarization current Js using a conjugate gradient method described in Ney [25]. This method is also described in appendix A.

$$Js_{mx1} = [\mathbf{M}]^{-1}_{mxn}\, Es_{nx1} \tag{3.21}$$

Once the polarization current is obtained, equation (3.10) can be used to calculate the internal scattered field. Since the points x and y are now inside the target domain, there is the possibility that during the integration the observation points x and y will equal the integration variables x' and y' resulting in a value of zero for ρ. Care must be taken when the observation point is the same as the integration point. When this happens, ρ is equal to zero which makes the Hankel function go to infinity. The integration over this patch does have a finite value which results in the special case for calculating the matrix for the external scattered field.

$$E_{scat}^{int}(x,y) = \int_s -\frac{j}{4} J_s(x,y) H_o^2(k_o \varrho) ds \tag{3.22}$$

Using the same steps as outlined earlier, this integral equation can be transformed into the following matrix equation:

$$E_{scat_{mx1}}^{int} = [\mathbf{N}]_{mxm} \; Js_{mx1} \tag{3.23}$$

where

$$\begin{aligned} \mathbf{N}_{ij} &= -\frac{j\pi a}{2k_o} J_1(k_o a) H_o^2(k_o \varrho) && i \neq j \\ \mathbf{N}_{ij} &= -\frac{j}{2k_o^2} [\pi k_o a H_1^2(k_o a) - 2j] && i = j \end{aligned} \tag{3.24}$$

where H_1^2 is the first order Hankel function of the second kind. To find the total field inside the target region, the incident field is added to the internal scattered field.

$$E_{tot} = E_{inc} + E_{scat}^{int} \tag{3.25}$$

Using equations (3.21) and (3.23) to substitute for E_{scat}^{int} gives

$$E_{tot} = Einc_{mx1} + [\mathbf{N}]_{mxm} \; [\mathbf{M}]_{mxn}^{-1} \; Es_{nx1} \tag{3.26}$$

Rearranging equation (3.11) to solve for the difference in propagation constants gives

$$-\frac{j}{\omega \mu_o} (k_s^2(x,y) - k_o^2) = \frac{Js_{mx1}}{Etot_{mx1}} \tag{3.27}$$

Substituting equation (3.21) and equation (3.26) for Js and E_{tot} respectively in equation (3.27) gives

$$-\frac{j}{\omega\mu_o}(k_s^2(x,y)-k_o^2) = \frac{[\mathbf{M}]^{-1}_{mxn}\ Es_{nx1}}{Einc_{mx1} + [\mathbf{N}]_{mxm}\ [\mathbf{M}]^{-1}_{mxn}\ Es_{nx1}} = S_{mx1} \tag{3.28}$$

where S is known as the contrast. The contrast can now be solved for the real and imaginary parts of complex permittivity by

$$\epsilon_{ri} = \mathrm{Re}\left\{\frac{S_i}{k_o^2} + 1\right\} \tag{3.29}$$

$$\epsilon_i'' = \mathrm{Im}\left\{\frac{S_i}{k_o^2}\right\} = \frac{\sigma}{\omega\ \epsilon_o} \tag{3.30}$$

Chapter 4 Results of Computer Simulation of Lossless Cylinders

In this chapter the results of the reconstructions of the various lossless dielectric cylinders are presented. The first sets of results presented are to confirm the results found in this thesis with the results of the numerical inverse scattering algorithm published in [24]. More computer simulations were carried out on other lossless dielectric cylinders in order to determine what effects selected variations in target cylinders had on the ability of the algorithm described in this thesis to calculate the dielectric cross section of the target cylinder. The different cases of target cylinders which were investigated were the position of a single scatterer in the target region, the number of patches in the target region, the size of target region, the dielectric permittivity of a single scatterer in the target region, and the dielectric constant of the entire target region with a single subscatterer.

The position of a single scatterer in the target region was moved to all of the possible positions in the positive y region of a selected test target region. Since the target region and the incident plane wave are symmetric about the x axis, only target positions in half of the region have to be investigated. The scattered field produced by the single scatterer is the same in all of the cases. However, the effect the position has on the reconstruction comes from the difference in where the scattered field is sampled with respect to the position of the scatterer. More specifically, the values for the elements in the matrices $\mathbf{M}$ and $\mathbf{N}$ will be different for each position because of the different values of $k_o\rho$ in the equations (3.20) and (3.24) which are used to fill the matrices.

Increasing the number of patches m in the target area increases both the number of elements in the matrix **N** by a factor of m^2, and the number of rows in the matrix **M** by a factor m. Therefore, an increase in the number of patches can have a large effect on the size of the matrices. The most noticeable effect is in the execution times which are proportional to the size of the matrices **M** and **N**. The other effect, which is an obvious one, is in the memory required to run the program. The most detrimental effect coming from the number of patches in the target region is on the numerical accuracy coming from the inversion of the matrix **M** in equation (3.21). When the target region is decreased, an improvement in the accuracy is noticed. This improvement is attributed to the fact that there are less unknown variables in the matrix equations.

The most sensitive parameter to the reconstruction is the dielectric permittivity of the target region. A large difference in the permittivity of the measurement region and the target region will produce an impedance mismatch which reduces the amount of power being coupled into and out of the target. However, for most lossless targets the amount of power being received from the target is enough to be able to carry out a reconstruction. It is believed that the dielectric constant of the target region also causes some phase error in the sampled scattered field because of the wavelength compression properties of the dielectric.

In order to compare the reconstructions of different cases, the following formula was used to associate each construction with a single number.

$$\alpha_{err} = \frac{\sqrt{\sum_{i=1}^{m}(\epsilon_{ri}^{cal} - \epsilon_{ri}^{orig})^2}}{\sqrt{\sum_{i=1}^{m}(\epsilon_{ri}^{orig})^2}} \tag{4.1}$$

where ϵ_{ri}^{cal} is the calculated dielectric constant, and ϵ_{ri}^{orig} is the original dielectric constant.

Generally, values for α_{err} less than 0.1 are considered to be good reconstructions while values up to 0.15 are acceptable and values higher than 0.15 are considered unacceptable.

4. 1 Validation of the Formulation

To validate the algorithm used in this thesis, results from a case run by Caorse, Gragnani, and Pastonino [24] were reproduced. This test case used a target region broken up into 25 patches. The sides of the area were 5/3λ and the length for the sides of the patches were 1/3λ. Figure 4.1 shows the test region.

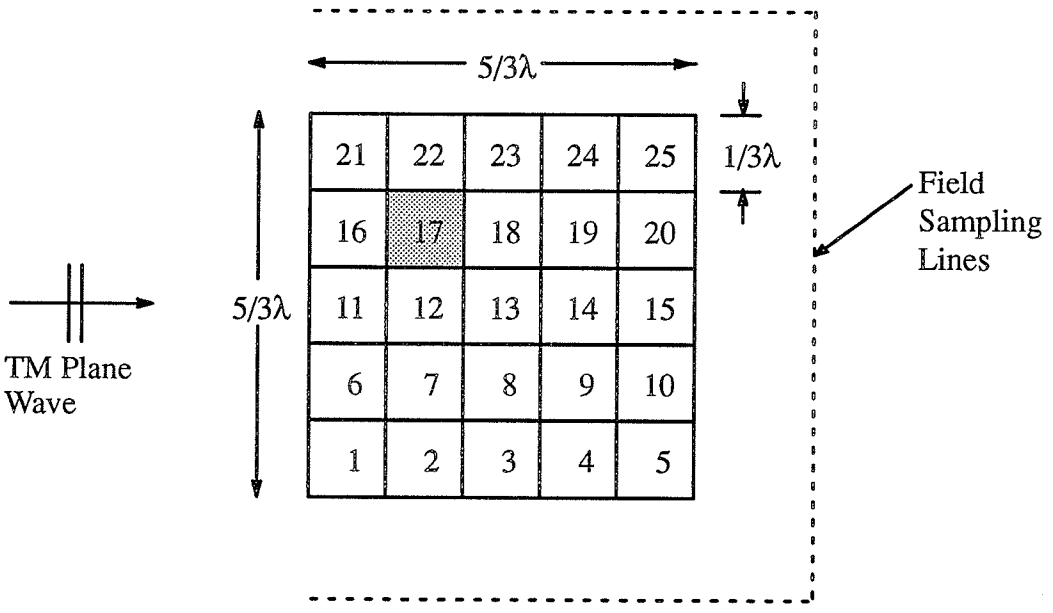

Fig. 4.1 – Test target.

In the test target a single scatterer was placed in position 17, and was given a dielectric constant of $\varepsilon_r^* = 3.0 - j\,0.0$. The rest of the target space was given a dielectric constant of $\varepsilon_r^* = 1.0 - j\,0.0$. The incident field was a TM plane wave propagating from the negative x direction. The scattered field was sampled along three lines along the top, bottom, and the positive x side of the target. These sampling positions were chosen so that the receivers would not interfere with the incident field approaching from the negative x direction.

Figure 4.2 shows the three dimensional type plot of the original test target that is used to display the data in this thesis.

NOTE: Because the plotting program used does not have the capability to label the axis with Greek letters, the label "er" will be used in place of "ε_r" in all of the figures.

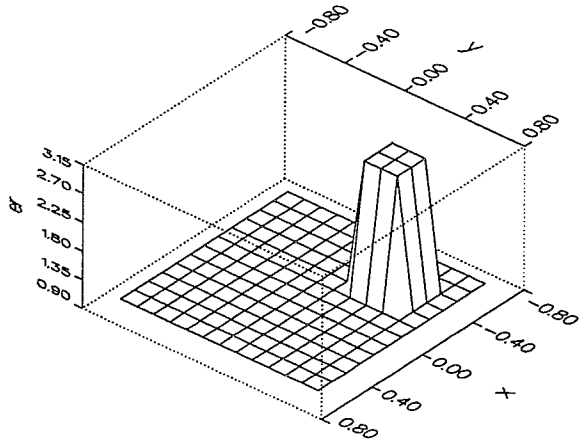

Fig. 4.2 – Original test target.

The results from [24] and the results that were found are shown in figures 4.3 and 4.4 respectively. For the results in figure 4.4, a sampling radius of $\rho = 2.0\lambda$ was used.

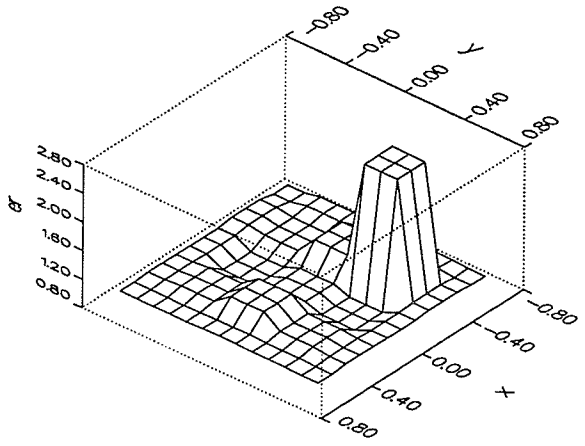

Fig. 4.3 – Test target reconstruction from [24].

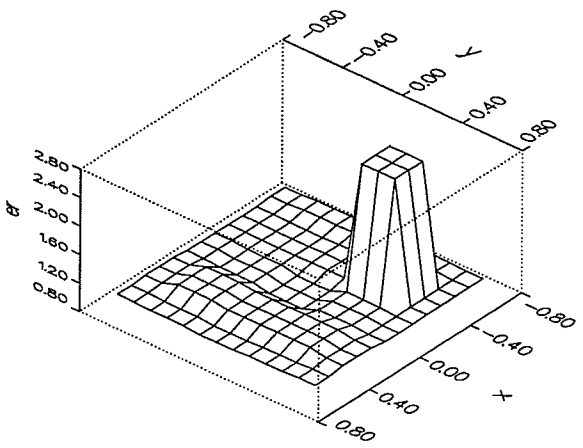

Fig. 4.4 – Thesis test target reconstruction.

For all intensive purposes, the results from the two techniques are the same. The value for α_{err} found by [24] was 0.09187; whereas the result found here for α_{err} was 0.06314. Furthermore, the final reconstructed value for the dielectric constant of the single scatterer found by [24] was $\varepsilon_r = 2.631$ while the result here was $\varepsilon_r = 2.686$. These discrepancies can be attributed to two factors. The first is the selection of the sampling points for the scattered field, and the second, the algorithms used to invert the matrix [**M**]. In the case of [24] the field was taken along straight lines on three sides of the object; whereas in this case the field was sampled at evenly distributed points around a circle. It was found here and in [27] that changing the position of the sampling points had a drastic effect on the overall result. Sampling along three sides of the target region leaves one side of the target region open so that the receivers will not interfere with the incident field. Although this consideration is a practical one, it was decided for the purpose of computer simulation not to use it in this instance so that a better idea of the best case performance of the algorithm could be obtained. The two types of inversion algorithms used, namely, the pseudoinverse and the conjugate

gradient method, produce a least squares solution. However, they are fundamentally different algorithms and not surprisingly produce slightly different results.

4. 2 Effects of Position of a Single Scatterer in a Free Space Target Region

This section shows the effects of the position of a single scatterer on the overall reconstruction. In figure 4.1, the position of the scatterer was moved to positions numbered 11 through 25. Since the target region and the incident field are symmetric about the x axis, only positions in the positive y region were investigated. The dielectric constant for the single scatterer was taken to be $\varepsilon_r^* = 3.0 - j\,0.0$, and the dielectric constant of the surrounding target region was taken to be the free space dielectric constant $\varepsilon_r^* = 1.0 - j\,0.0$. The results of each position are shown in figures 4.5 to 4.18, and the results are summarized in table 4.1.

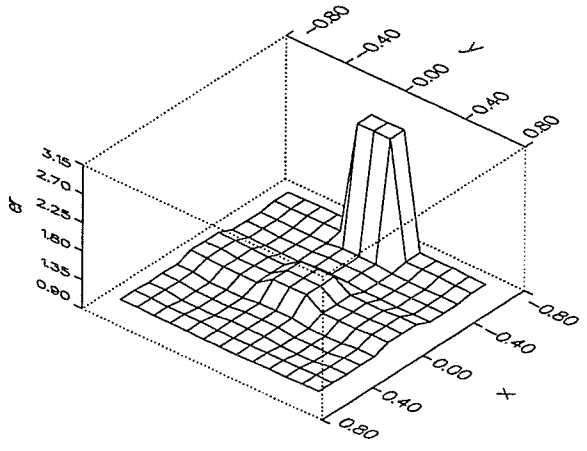

Fig. 4.5 – Results for position 11.

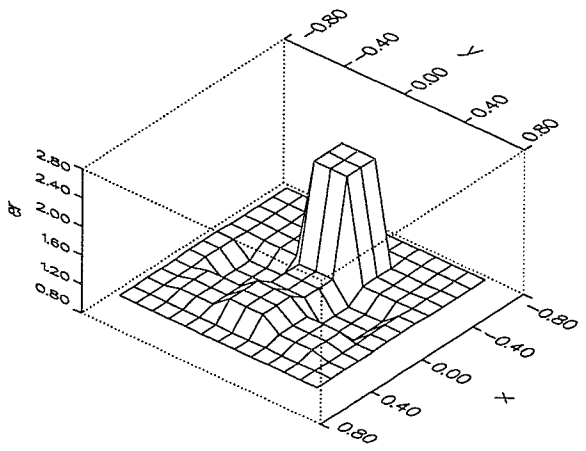

Fig. 4.6 – Results for position 12.

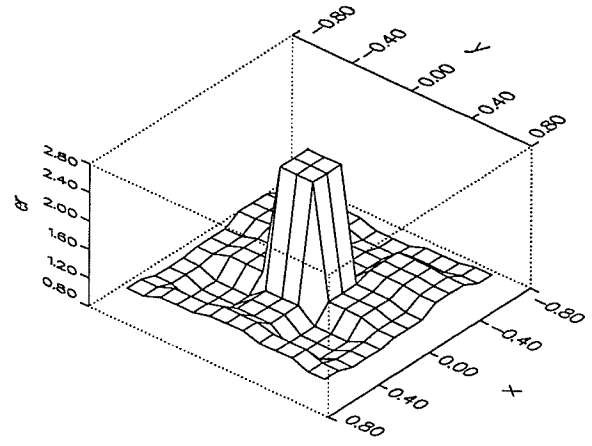

Fig. 4.7 – Results for position 13.

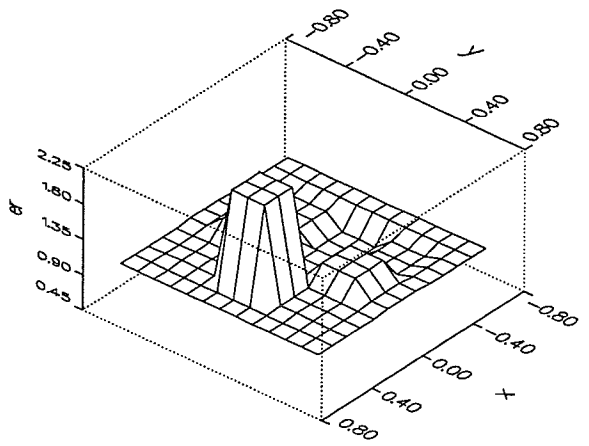

Fig. 4.8 – Results for position 14.

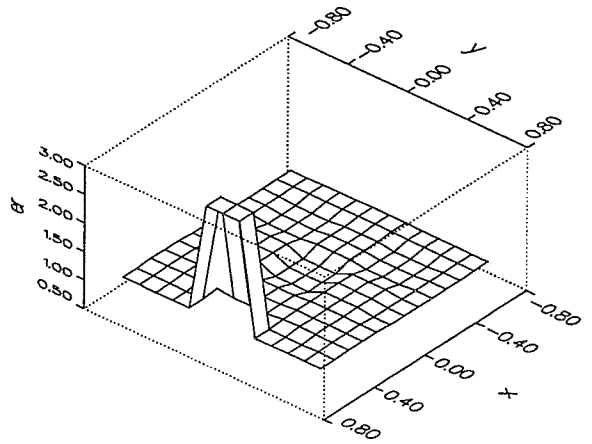

Fig. 4.9 – Results for position 15.

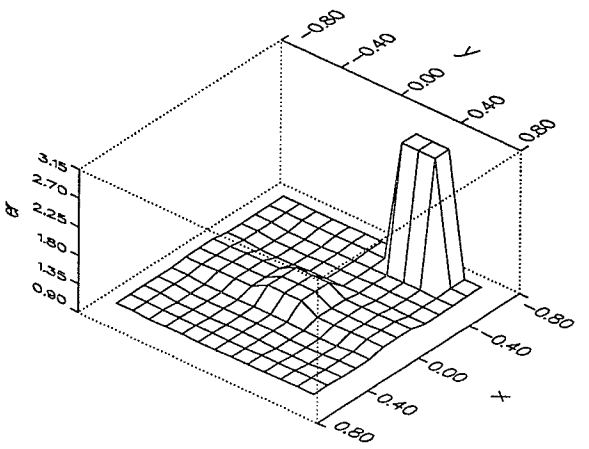

Fig. 4.10 – Results for position 16.

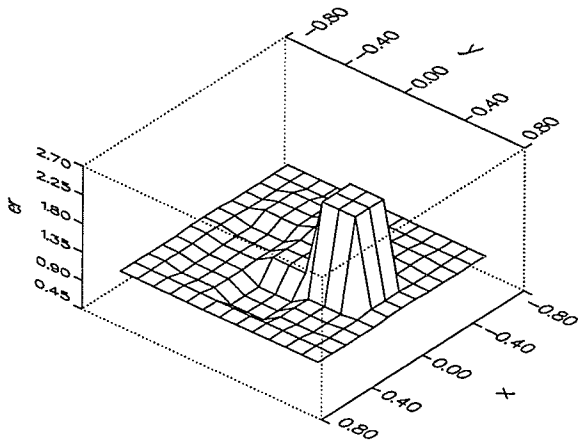

Fig. 4.11 – Results for position 18.

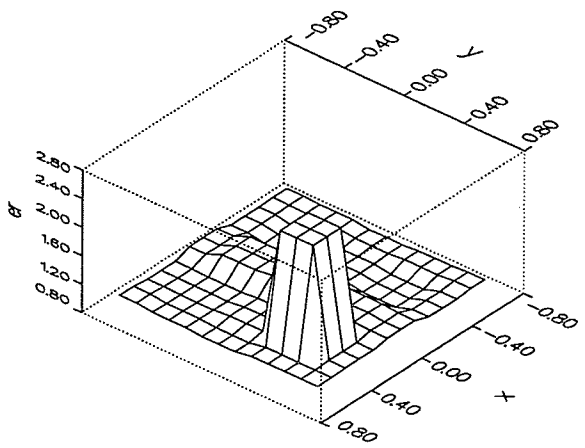

Fig. 4.12 – Results for position 19.

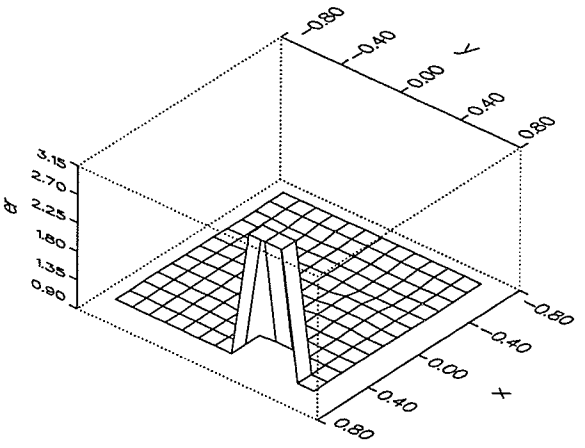

Fig. 4.13 – Results for position 20.

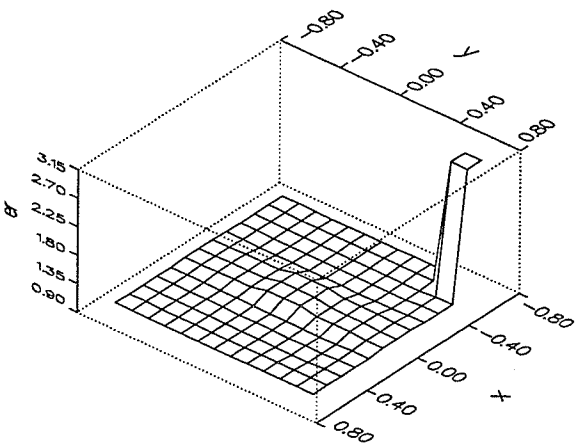

Fig. 4.14 – Results for position 21.

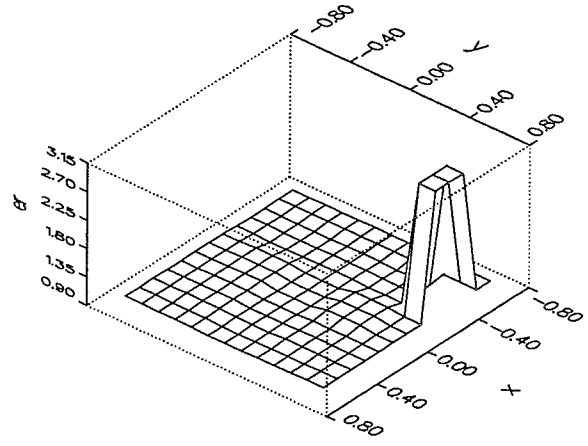

Fig. 4.15 – Results for position 22.

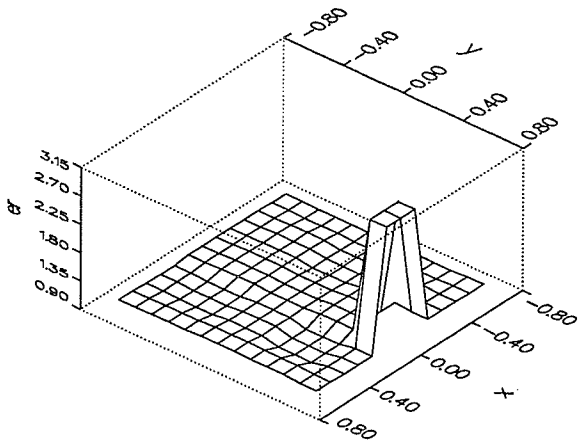

Fig. 4.16 – Results for position 23.

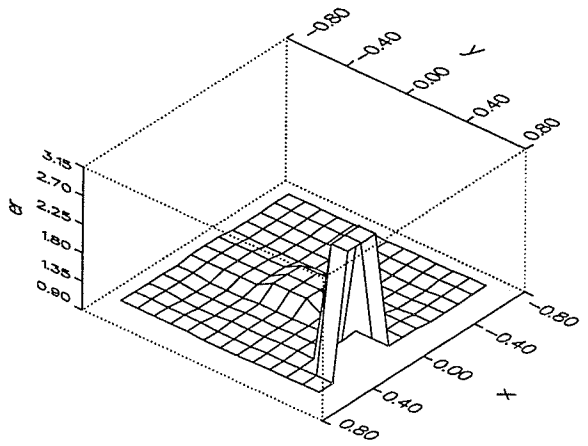

Fig. 4.17 – Results for position 24.

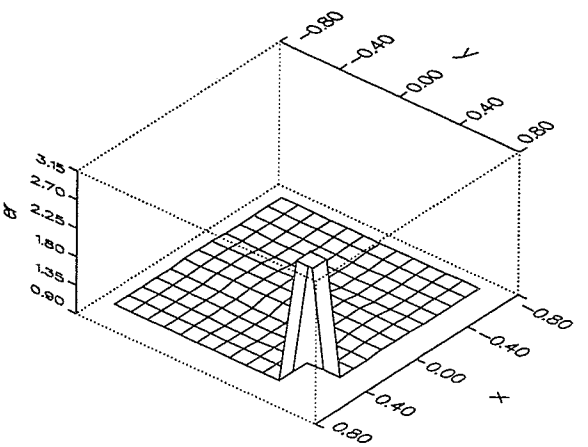

Fig. 4.18 – Results for position 25.

Position	ε_r Calculated for patch 17	error α_{err}
11	2.810	0.057
12	2.400	0.122
13	2.631	0.101
14	2.186	0.048
15	2.907	0.028
16	2.933	0.037
17	2.686	0.063
18	2.351	0.126
19	2.507	0.102
20	2.983	0.011
21	2.994	0.019
22	2.985	0.013
23	2.889	0.027
24	2.935	0.036
25	3.003	0.012

Table 4.1 – Results summary for various positions.

The results in table 4.1 show that the best results are obtained when the scatterer is along the edge of the target region in positions 11, 15, 16, and 20, and in 21 to 25. The result with the lowest error was obtained when the scatterer was in position 20. On the other hand, when the scatterer was in the interior cells 12 to 14 and 17 to 19, the results were not as good. The result with the greatest error was obtained when the scatterer was in position 18. An explanation for these results could be the distance between the interior points and the points where the scattered field is sampled. As previously mentioned, the radius at which the scattered field is sampled should be as small as possible. This is done to produce the largest possible differences in the phase and amplitude in the signals being received from each patch

during the summation carried out in equation (3.13). This will generate the greatest independence between the columns in the matrix **M**.

4. 3 Effects of Discretization

To demonstrate the effects of different discretizations on the results of the algorithm, two types of changes were made to the discretization of the original test target in figure 4.2. The first set of results were generated by increasing the number of patches in the target region. This was done by reducing the size of the patches which resulted in having four times and nine times as many patches in the original test target. This is an important property to investigate since the patch size directly dictates the resolution obtained in the reconstruction of the cylinder. The other type of change in the discretization was the reduction of the free space surrounding the single scatterer. In this case, the total number of unknowns was reduced; whereas the number of points sampled from the scattered field was constant, making the equation (3.19) overdetermined.

4. 3. 1 Increased Discretization

In this section the results for discretizations with an increasing number of patches are presented. Figure 4.2 shows the discretization used to generate the first set of results. The next set of results were generated using a discretization which had four times as many patches; whereas the size of the target area and scatterer remained the same. In this case, the length of the sides of the patches was one half of the length in the first discretization. The last set of results was produced using a discretization which has nine times as many patches as the original discretization shown in figure 4.2. For this discretization the length

of the sides of the patches was one third of the original patch side length. These two discretizations are shown in figures 4.19 and 4.20.

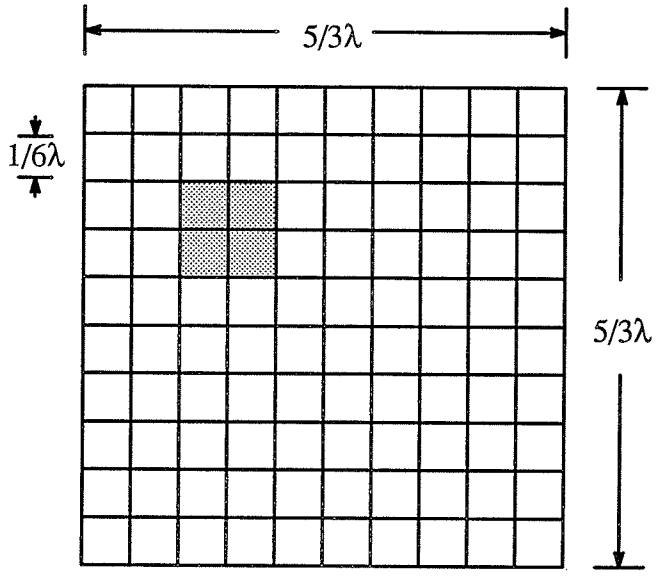

Fig. 4.19 – 100 patch discretization.

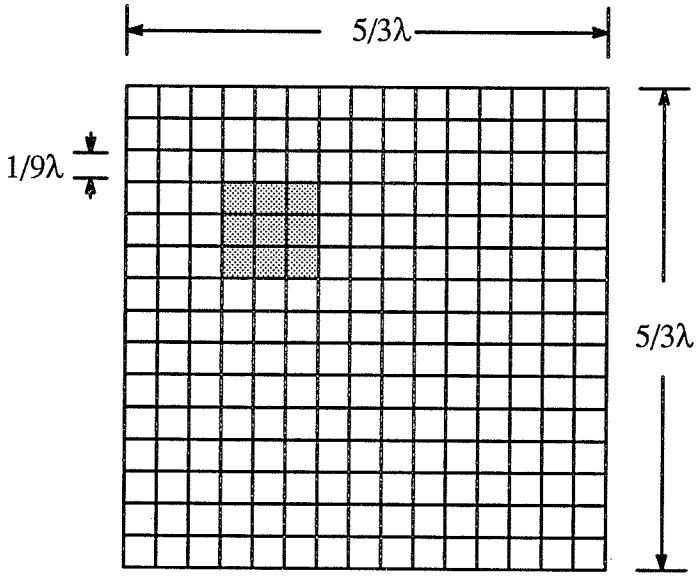

Fig. 4.20 – 225 patch discretization.

Figures 4.21 to 4.23 show the results for each of the three cases. In each figure, (a) shows the original target arrangement and (b) shows its reconstruction.

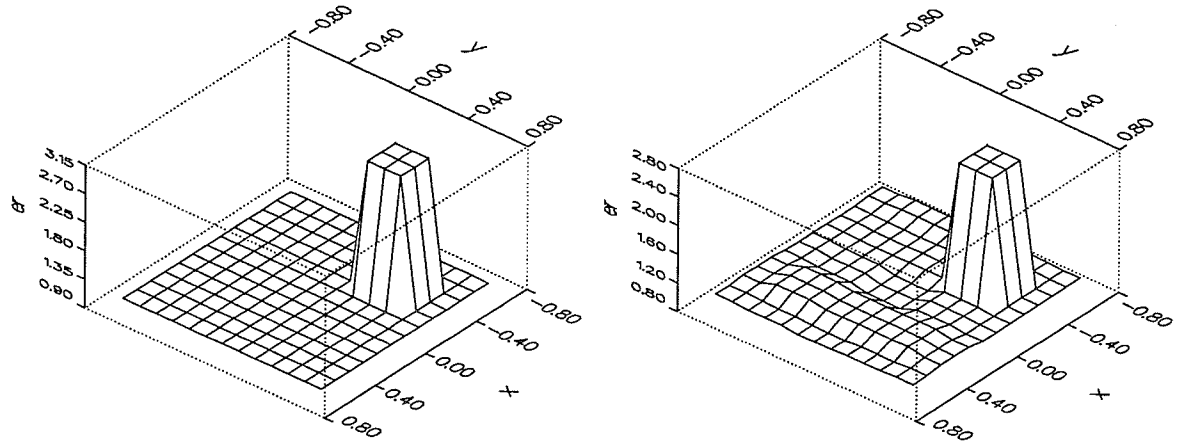

(a) Original target (b) Reconstruction

Fig. 4.21 – Discretization with 25 patches.

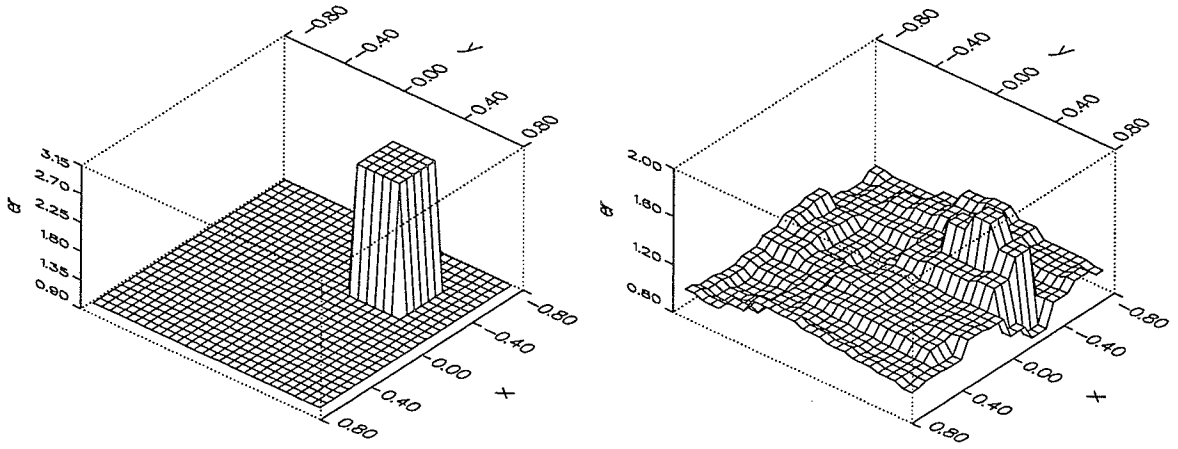

(a) Original target (b) Reconstruction

Fig. 4.22 – Discretization with 100 patches.

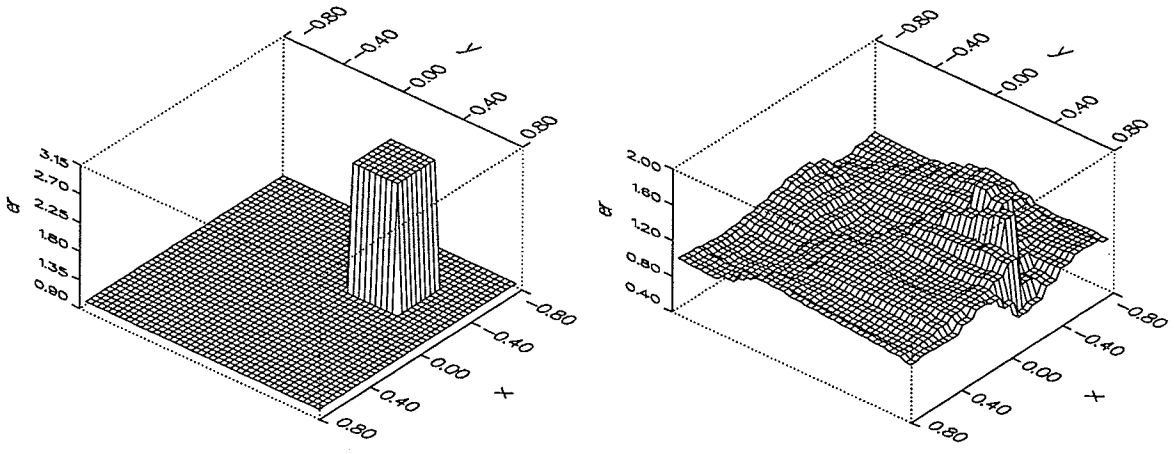

(a) Original target (b) Reconstruction

Fig. 4.23 – Discretization with 225 patches.

In all the cases, the results show the position of the single scatterer quite well. However, with the increased discretization, the value of the dielectric constant goes from 2.686 to 1.611 to 1.617. Meanwhile, the value for the accuracy α_{err} goes from 0.063 to 0.302 to 0.298. These results show a flattening of the accuracy, or a point of diminishing returns, in the calculation of the dielectric constant value and the overall accuracy. The reliability of the reconstruction in the case of increasing the discretization is limited by both the determination of the position of the single scatterer and by the calculation of its dielectric constant. Unfortunately, a problem with stack size prohibited the generation of any results with more than 225 patches.

4. 3. 2 Effects of Decreasing the Free Space Target Region Around a Single Scatterer

In this section the size and total number of patches in the target region was decreased by reducing the amount of free space in the target region. Since all patches except patch 17 shown in figure 4.1, have the dielectric constant of free space $\varepsilon_r^* = 1.0 + j\,0.0$, they can be systematically eliminated until only the area occupied by patches corresponding to patch 17 are being imaged. The results begin with the target region shown in figure 4.23 (a), where the total number of patches is 225. The area surrounding patch 17 was then decreased until only the 9 patches on the single scatterer remained.

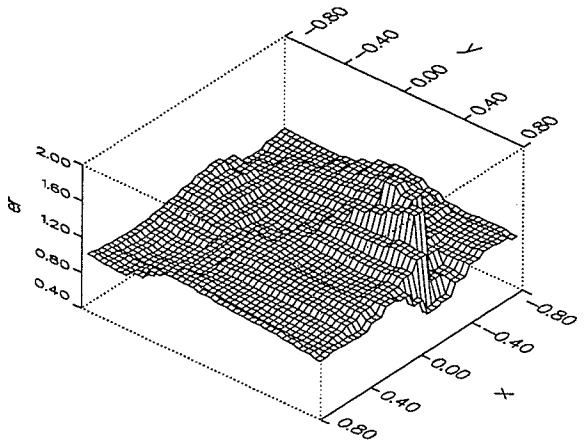

Fig. 4.24 – Reconstruction of full target area with 225 patches.

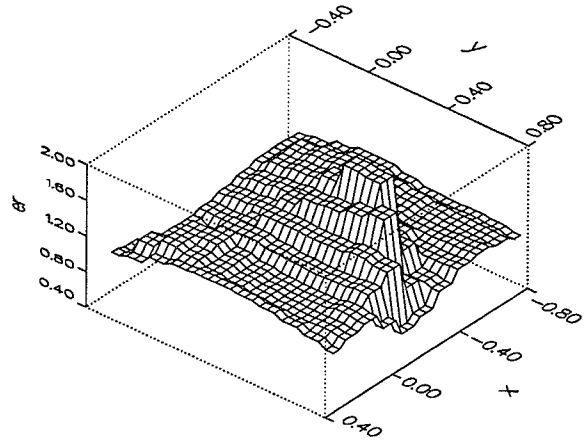

Fig. 4.25 – Reconstruction of the decreased target area with 112 patches.

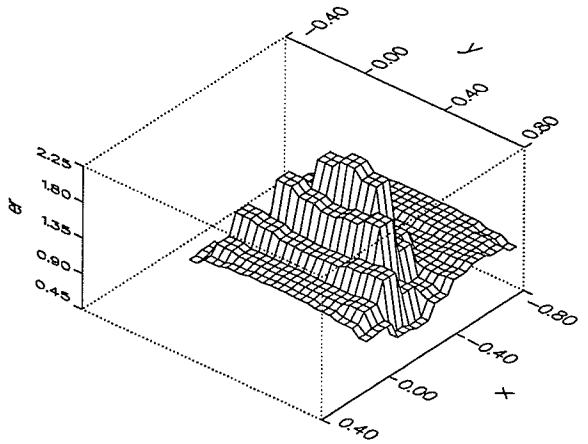

Fig. 4.26 – Reconstruction of the decreased target area with 81 patches.

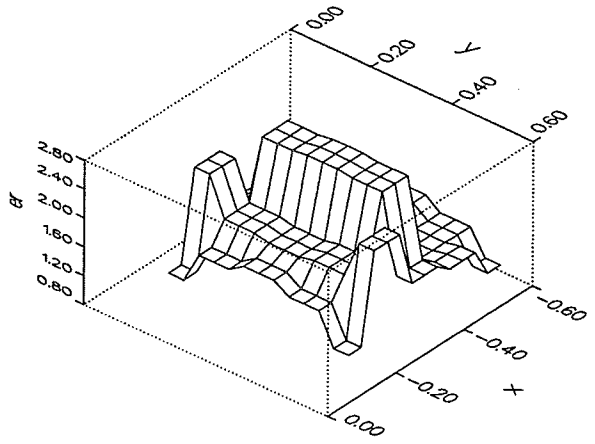

Fig. 4.27 – Reconstruction of the decreased target area with 25 patches.

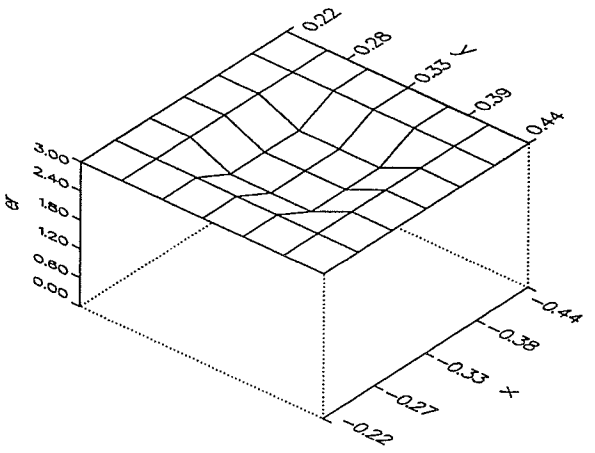

Fig. 4.28 – Target area of the single scatterer with 9 patches.

For each result of a decreased target space there is an increase in the calculation of the dielectric constant of the target. In figure 4.28 where only the single scatterer occupies the target region, the reconstruction is almost perfect. The reason for this result comes from the fact that as the total number of unknowns is reduced, equation (3.19) becomes over determined, and the problems with the matrix M being ill–conditioned are reduced.

4. 4 Dielectric Permittivity Effects

In this section the effects of the dielectric permittivity are examined. There are two cases presented here. First, the permittivity of a single scatterer is varied, and secondly, the dielectric permittivity of the area surrounding a single scatterer is changed.

Varying the dielectric constant has the effect of changing the intrinsic impedance of the target media. This creates an impedance mismatch which makes it difficult to couple power into the target. The formula for the intrinsic impedance is

$$\eta = \sqrt{\frac{\mu}{\epsilon}} \tag{4.2}$$

From equation (4.2) the relationship between the intrinsic impedance η and the dielectric constant ε is an inverse square root relationship.

4. 4. 1 Increased Target Dielectric Constant

This section presents the results from cases where the dielectric constant of only a single scatterer in the target region is increased. This set of results was generated using the discretization shown in figure 4.1. As done in previous sections, the single scatterer was located at patch 17. The dielectric constant of the patch was then increased from $\varepsilon_r^* = 1.5 - j\,0.0$ to $\varepsilon_r^* = 10.0 - j\,0.0$. These results for $\varepsilon_r^* = 1.5 - j\,0.0$ to $\varepsilon_r^* = 5.0 - j\,0.0$ are shown in figures 4.29 to 4.36, and are summarized in figures 4.37 and 4.38.

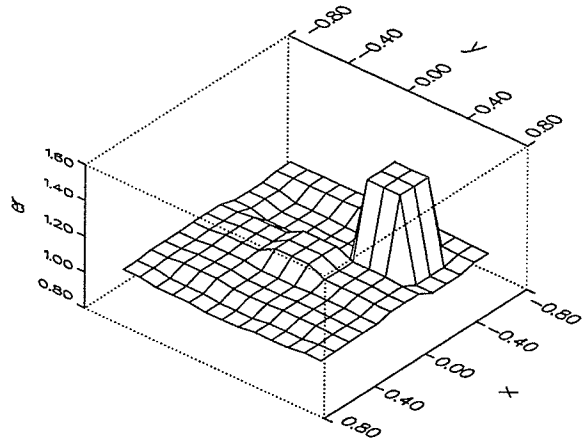

Fig. 4.29 – Results from $\varepsilon_r 17 = 1.5$.

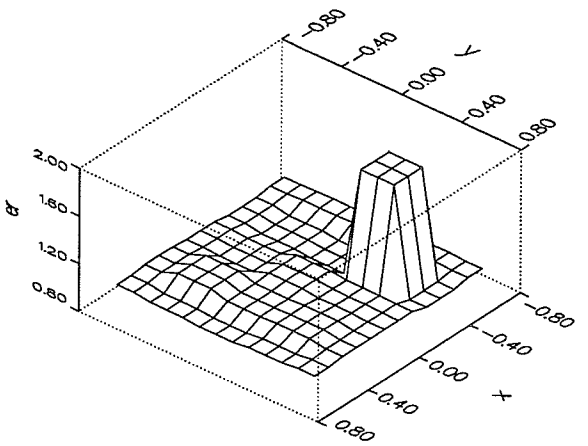

Fig. 4.30 – Results from $\varepsilon_r 17 = 2.0$.

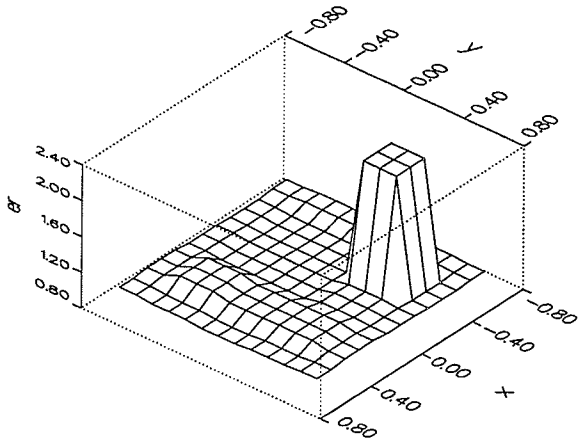

Fig. 4.31 – Results from $\varepsilon_r 17 = 2.5$.

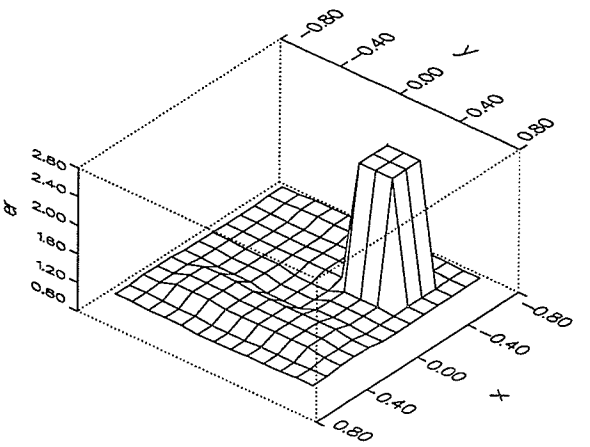

Fig. 4.32 – Results from $\varepsilon_r 17 = 3.0$.

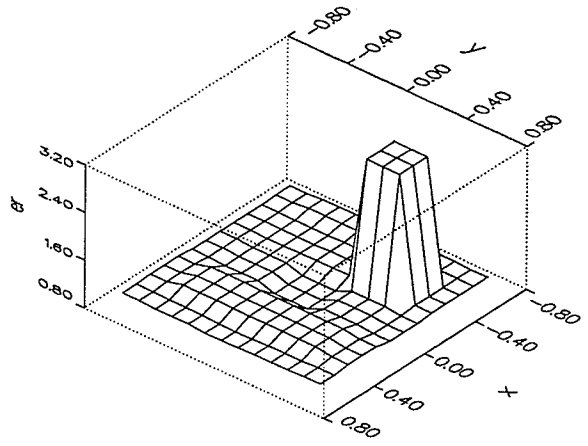

Fig. 4.33 – Results from $\varepsilon_r 17 = 3.5$.

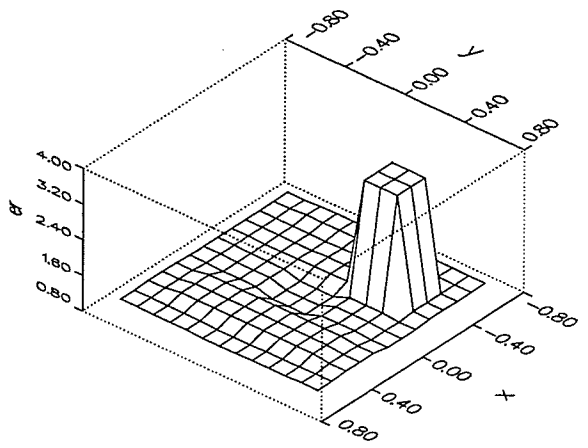

Fig. 4.34 – Results from $\varepsilon_r 17 = 4.0$.

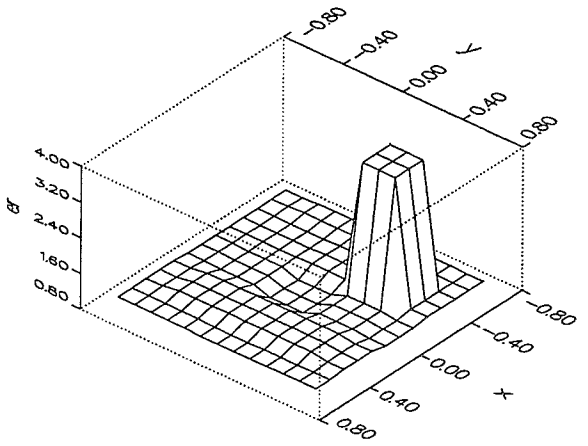

Fig. 4.35 – Results from $\varepsilon_r 17 = 4.5$.

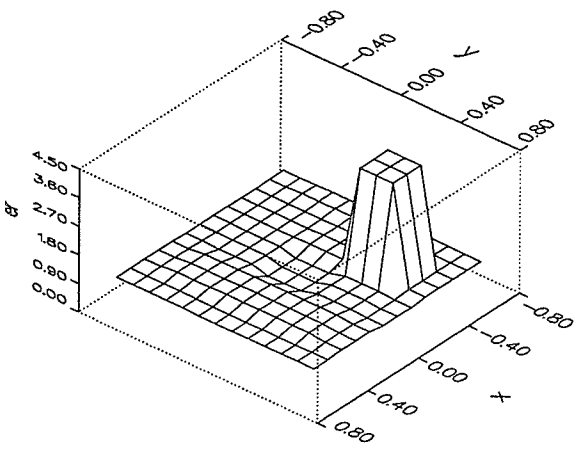

Fig. 4.36 – Results from $\varepsilon_r 17 = 5.0$.

The above results show a decreasing ability to calculate the dielectric constant of the scatterer as its value increases. However, the position of the scatterer is calculated accurately. Figure 4.37 is a graph of the calculated dielectric constant of patch 17 versus the actual dielectric constant of patch 17 as the dielectric constant is increased. Furthermore, in figure 4.38, the error α_{err} in the reconstruction is graphed versus the dielectric constant of patch 17.

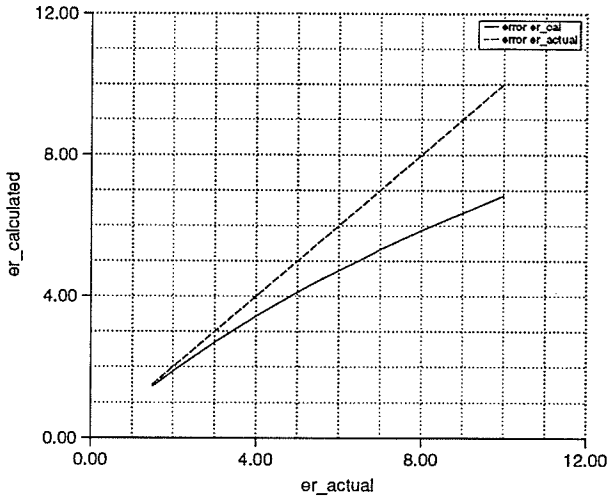

Fig. 4.37 – Graph of actual dielectric constant and calculated dielectric constant of patch 17.

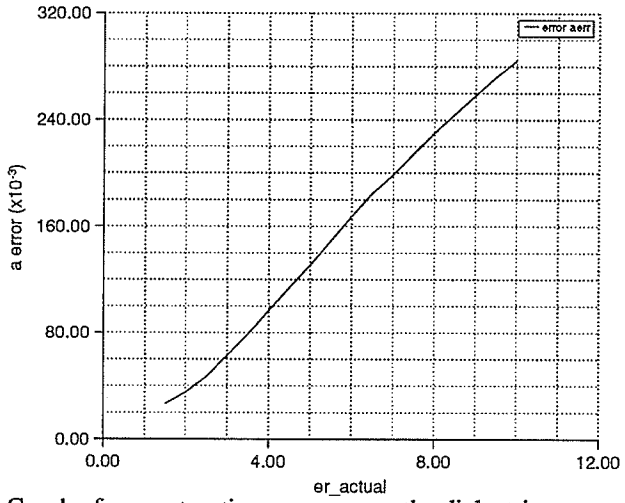

Fig. 4.38 – Graph of reconstruction error versus the dielectric constant of patch 17.

As shown in figure 4.38, the error appears to increase linearly with the increasing dielectric on patch 17. In the case where the dielectric constant of the single scatterer is increased, the accuracy of the reconstruction is limited by the ability to calculate the dielectric constant.

4. 4. 2 Effect of Dielectric Constant of the Total Target Region with a Single Scatterer Present

In this section the results from deviations in the dielectric permittivity of the target region are investigated. In previous results, the target region was mostly free space with a single scatterer occupying a single position. This type of scenario is not applicable for most practical applications. In most applications, there is some type of unknown dielectric cross section which has to be obtained. For this section the entire target region becomes a scatterer because its dielectric constant no longer equals the dielectric constant of the measurement region, and the single scatterer at position 17 now becomes a subscatterer within the target region.

In this case the intrinsic impedance of the target region becomes an important factor because there are now many unknown regions that have to be probed by the incident field. As the dielectric permittivity of the target region is increased, the amount of power being coupled into the region decreases as a result of the impedance mismatch between the target region and the free space where the incident field originates. Furthermore, the internal scattered field will encounter the same dielectric mismatch when exiting the target region, resulting in power being reflected back into the target region.

For this set of results the subscatterer is given a dielectric constant of $\varepsilon_r^* = 3.0 - j\,0.0$ while the dielectric constant of the surrounding target space is increased form $\varepsilon_r^* = 1.25 - j\,0.0$ to $\varepsilon_r^* = 2.25 - j\,0.0$. The results of these reconstructions are shown in figures 4.39 to

4.43. The incident field is still a TM plane wave incident from the negative x direction, and the scattered field is sampled at a radius of 2.0λ.

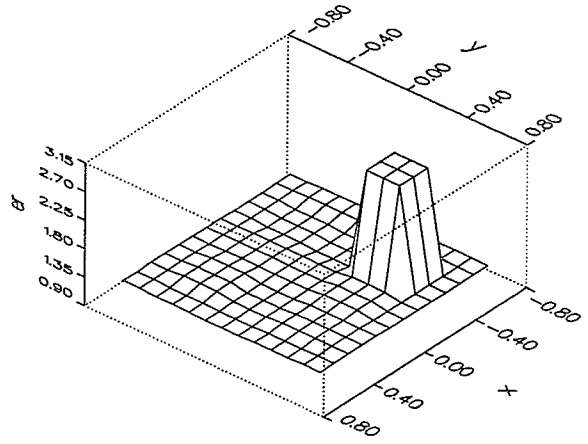

Fig. 4.39 – Target space dielectric $\varepsilon_r = 1.25$.

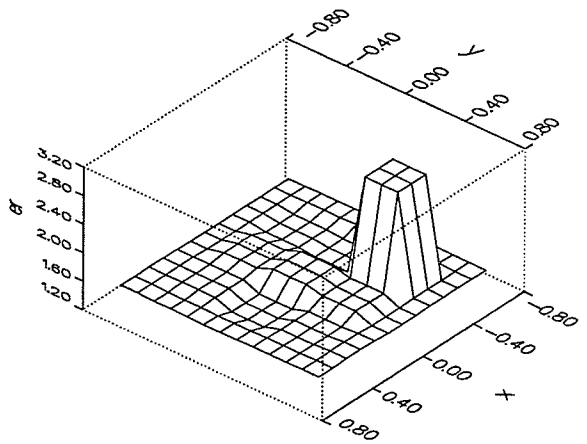

Fig. 4.40 – Target space dielectric $\varepsilon_r = 1.50$.

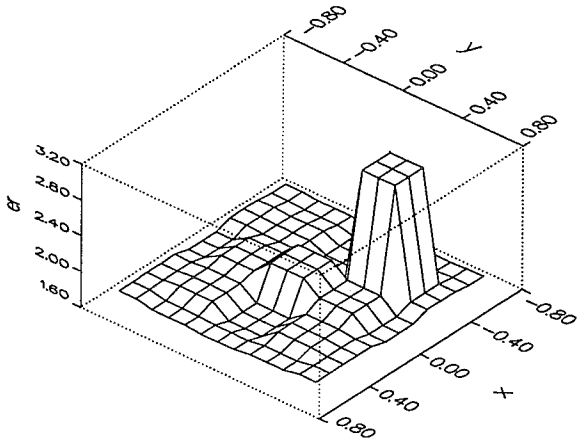

Fig. 4.41 – Target space dielectric $\varepsilon_r = 1.75$.

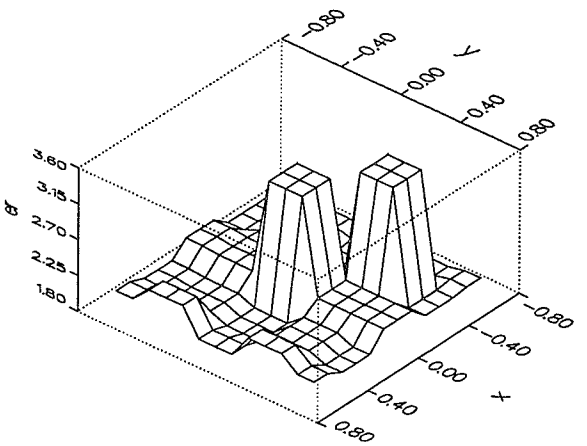

Fig. 4.42 – Target space dielectric $\varepsilon_r = 2.00$.

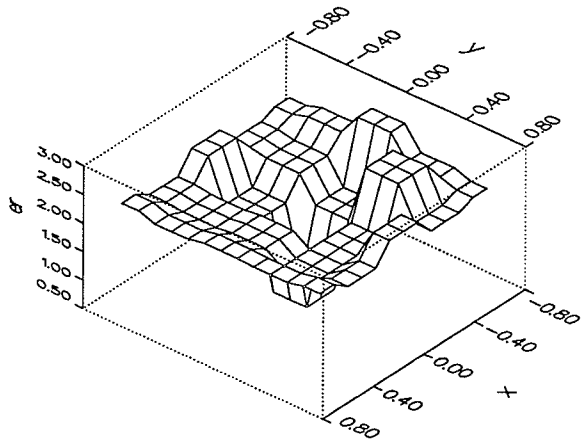

Fig. 4.43 – Target space dielectric $\varepsilon_r = 2.25$.

Figure 4.44 shows the dielectric constant of the subscatterer located at patch 17 versus the dielectric constant of the target space. The figure shows the value of ε_r for the scatterer is calculated with reasonable accuracy until the value of the dielectric constant of the target space reaches a value of 2.75. However, from figures 4.42 and 4.43 where the dielectric constant of the target space is 2.0 and 2.25 respectively, it can be seen that the position of the scatterer is not calculated reliably. Therefore, the algorithm in this case is limited by the ability to calculate the position of the single scatterer. Figure 4.45 shows the error for the reconstructions when the dielectric constant of the target space is increased from 1.25 to 4.0. This figure also shows the error increasing wildly for increasing values of the dielectric for the target region.

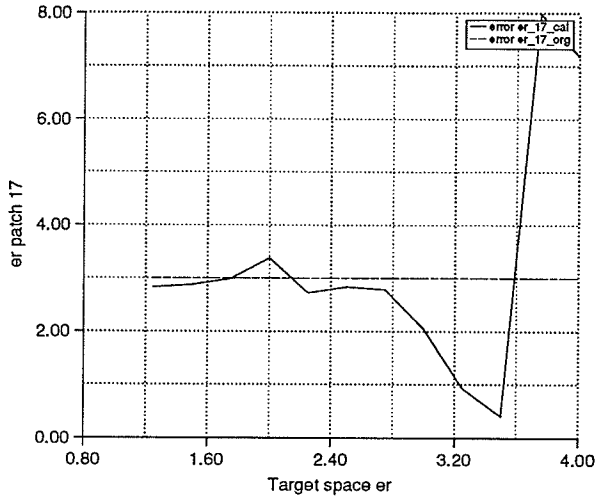

Fig. 4.44 – Subscatterer ε_r versus target space dielectric constant ε_r.

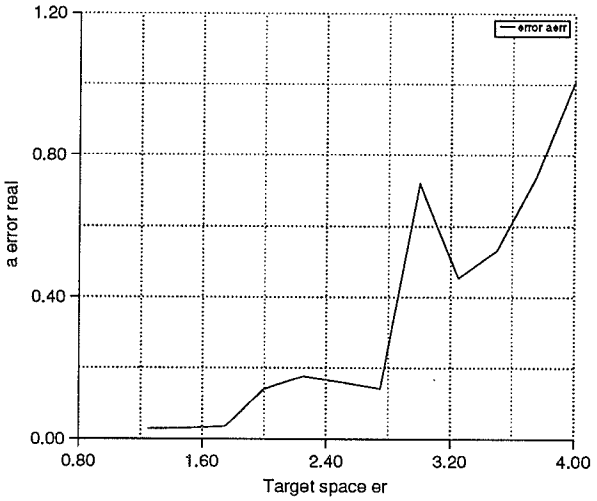

Fig. 4.45 – Error versus target space dielectric constant ε_r.

The problems associated with an impedance mismatch exist in the cases studied in subsection 4. 4. 1 ; however, the results in figures 4.39 to 4.43 show that the effect of the increasing dielectric permittivity of the target region appears to be much more severe in this section. In figures 4.42 and 4.43, when the dielectric permittivity of the target space is ε_r^* = 2.0 –j 0.0 and 2.25 – j 0.0 respectively, the results of the reconstruction are unacceptable. In subsection 4. 4. 1 however, the dielectric constant of the single scatterer can go as high

as $\varepsilon_r^* = 5.0 - j\ 0.0$ before the overall error α_{err} becomes comparable to the error obtained when ε_r^* of the target region equals $2.0 - j\ 0.0$. The reasons for differences in these results are not known exactly. However, one can speculate that the wavelength compression caused by the higher dielectric constant is creating some type of phase error in the scattered field. As mentioned before, the sampling radius should be made as small as possible in order to maximize the difference in the magnitude and phases of the fields measured at the sampling points. Increasing the dielectric constant of the target region has the effect of increasing the distance, in terms of wavelengths, from the center of the target region to the sampling radius because of the wavelength compression caused by the high dielectric. Some support for this claim comes from one case where the reconstruction improved after the sampling radius was decreased from 2.0λ to 1.2λ. In this case, the same target region used to generate the results shown in figure 4.42 was used again but with a sampling radius of 1.2λ instead of 2.0λ. The target in question had a target space dielectric constant of $\varepsilon_r = 2.0 - j\ 0.0$. The results of the reconstruction using the shorter sampling radius are shown in figure 4.46.

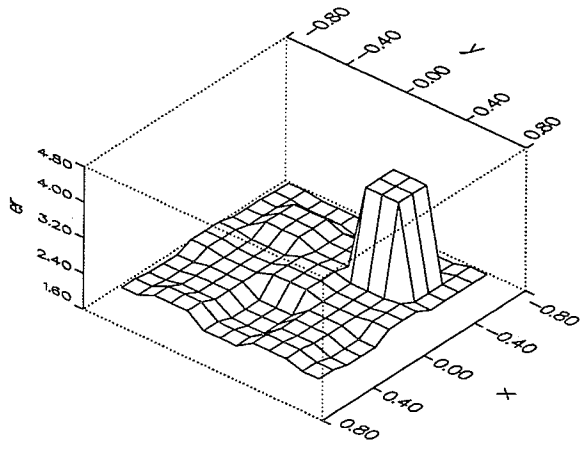

Fig. 4.46 – Target space dielectric $\varepsilon_r = 2.0$, and sampling radius of $1.2\ \lambda$.

The value for α_{err} for the above case was 0.11456 which is a noticeable improvement over the value of 0.014139 obtained when using the larger sampling radius. Furthermore, a comparison of the two figures shows the elimination of the false scatterer produced at the center of the target in figure 4.42.

Chapter 5 Computer Simulation Results From a Lossy Cylinder

In this section, lossy dielectric cylinders (conducting dielectric cylinders) are studied. In most of the applications of microwave imaging, the targets involved will have a dielectric permittivity and conductivity. In this section, the problems created by a high dielectric permittivity will still exist. In addition to these problems there will be others created by the loss of the cylinder or the conductivity.

The relationship between the conductivity of a material and the effect it has on an electromagnetic wave is an exponential one. The following equation is used to describe a time–varying electromagnetic plane wave.

$$E(x,t) = \mathrm{Re}\{E_o\, e^{(kx+j\omega t)}\} \tag{5.1}$$

Equation (5.1) can be rearranged in terms of an attenuation constant α and propagation constant β.

$$E(x,t) = e^{-\alpha x}\,\mathrm{Re}\{E_o\, e^{(\beta x+j\omega t)}\} \tag{5.2}$$

where α and β can be written in terms of the material parameters ε, σ, and μ [28].

$$\alpha = \omega \sqrt{\frac{\mu\epsilon}{2}\left[\sqrt{1+\frac{\sigma^2}{\omega^2\epsilon^2}}-1\right]} \tag{5.3}$$

$$\beta = \omega \sqrt{\frac{\mu\epsilon}{2}\left[\sqrt{1+\frac{\sigma^2}{\omega^2\epsilon^2}}+1\right]} \tag{5.4}$$

Using the complex dielectric notation ε_r^* described in section 3. 1, equations (5.3) and (5.4) become

$$\alpha = \omega \sqrt{\frac{\mu \epsilon'}{2} \left[\sqrt{1 + \frac{\epsilon''^2}{\epsilon'^2}} - 1 \right]} \tag{5.5}$$

$$\beta = \omega \sqrt{\frac{\mu \epsilon'}{2} \left[\sqrt{1 + \frac{\epsilon''^2}{\epsilon'^2}} + 1 \right]} \tag{5.6}$$

From equation (5.2) it can be seen that α is an attenuation constant for the exponential term and that attenuation α is also zero when the conductivity σ is zero. When σ is not zero, not only does it contribute to the attenuation, it also brings the dielectric constant ε into the calculation of the attenuation.

The loss in dielectric cylinders poses a number of problems to microwave imaging techniques. One is the fact that the loss in targets is proportional to the frequency; therefore, the higher the frequency of the incident field, the higher the loss is in the cylinder. High loss factors in targets prevent the incident signal from penetrating the interior of the targets. Consequently, no representation of the interior of the target will be present in the scattered field. Furthermore, discontinuities in the loss profile of the target cylinder will create impedance mismatch losses between the target region and the measurement region.

In the case of the algorithm presented in this thesis, the high loss poses another complication. In equation (3.27) in Chapter 3, the polarization current J_s is divided by the total electric field E_{tot} which gives the difference in propagation constants or the contrast *S*.

If the total field E_{tot} is zero or if it becomes numerically close to zero, the division will result in an erroneous answer. If the attenuation in a cylinder is very high, then the total electric field on the patches in the center could become zero which would result in the previously described phenomena.

5.1 Results for a Single Lossy Target

The results posted here are from a single lossy cylinder within the target region. The single scatterer was located at position 17 as was done in subsections 4. 4. 1 and 4. 4. 2 . In this case, the results are not affected too dramatically by the increasing loss. The results found this time, as the results found in subsection 4. 4. 1 , did not affect either the ability of the algorithm to determine the position of the single scatterer, or the calculation of the dielectric properties of the target space. There was however, an effect in the ability to calculate the dielectric constant of the single scatterer.

The results were generated by using the same target shown in figure 4.1. The complex part of the dielectric constant for patch 17 was increased from $\varepsilon_r = 3.0 - j\ 1.5$ to $\varepsilon_r = 3.0 - j\ 10.0$ while the dielectric constant of the rest of the target region was held constant at $\varepsilon_r = 1.0 - j\ 0.0$. Examples of the results are shown in figures 5.1 to 5.5.

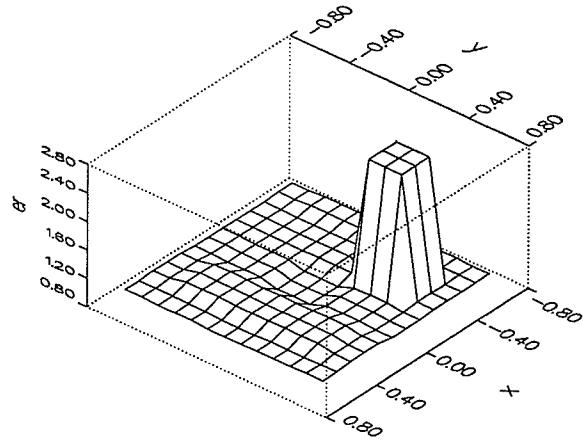

(a) Dielectric reconstruction

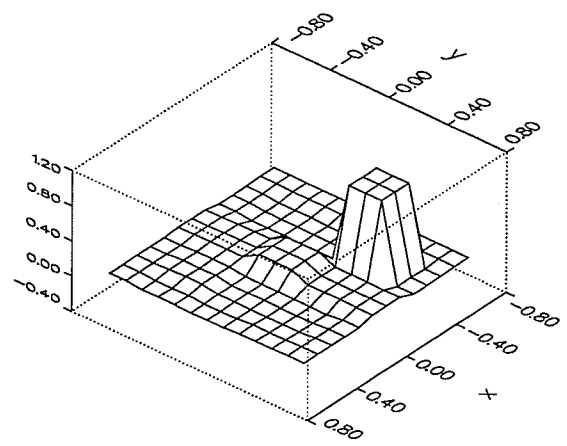

(b) Loss factor reconstruction

Fig. 5.1 – Reconstruction of a single subscatterer with a dielectric constant of $\varepsilon_r = 3.0 - j\ 1.0$.

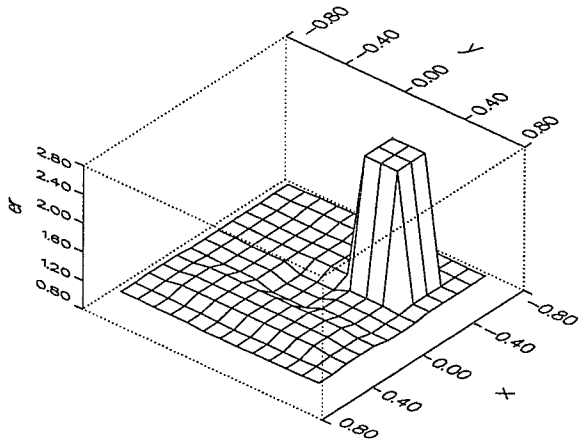

(a) Dielectric reconstruction

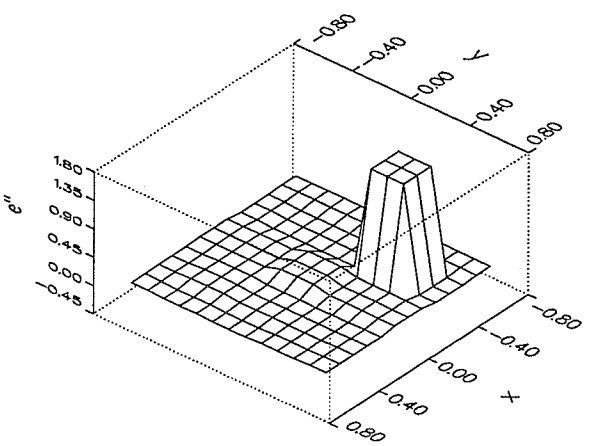

(b) Loss factor reconstruction

Fig. 5.2 – Reconstruction of a single subscatterer with a dielectric constant of $\varepsilon_r = 3.0 - j\ 2.0$.

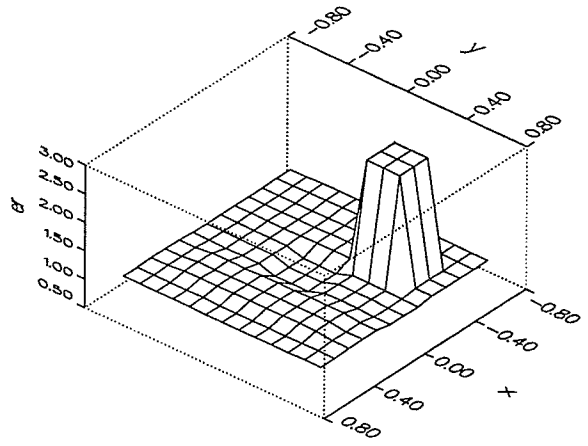

(a) Dielectric reconstruction

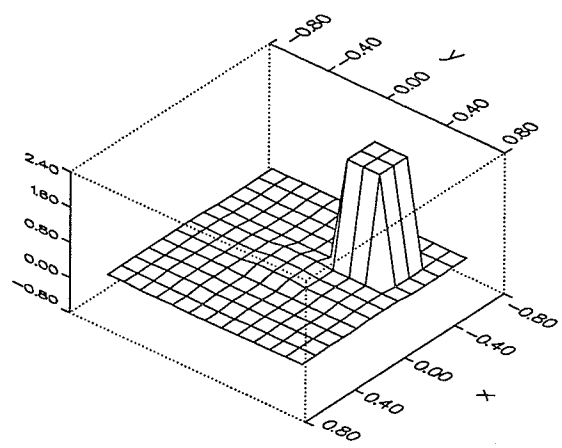

(b) Loss factor reconstruction

Fig. 5.3 – Reconstruction of a single subscatterer with a dielectric constant of $\varepsilon_r = 3.0 - j\,3.0$.

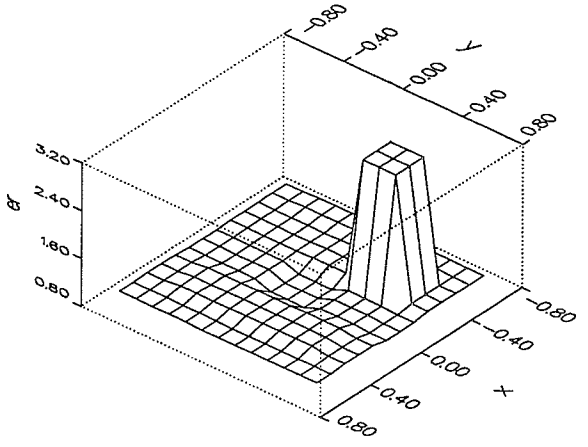

(a) Dielectric reconstruction

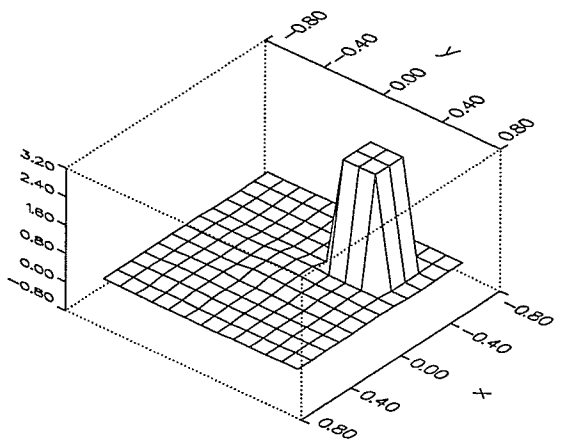

(b) Loss factor reconstruction

Fig. 5.4 – Reconstruction of a single subscatterer with a dielectric constant of $\varepsilon_r = 3.0 - j\,4.0$.

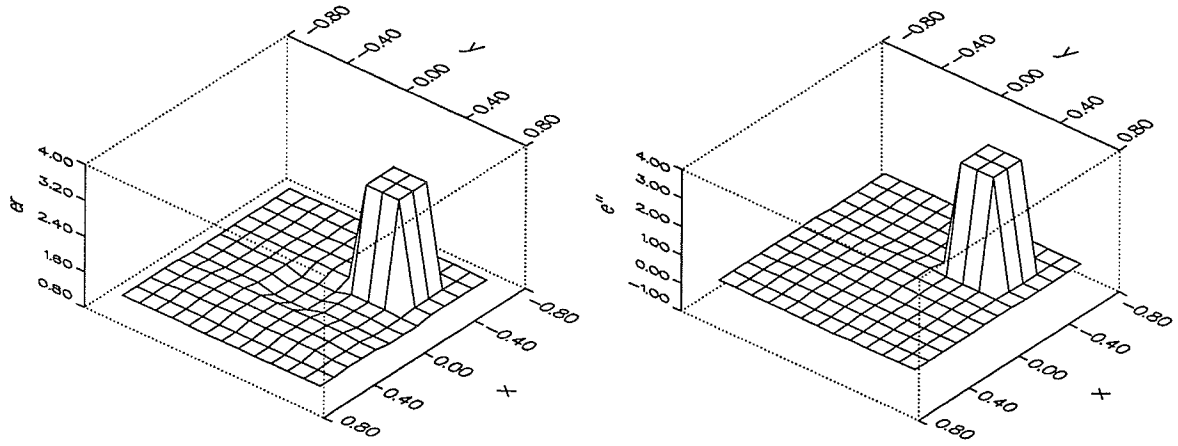

(a) Dielectric reconstruction (b) Loss factor reconstruction

Fig. 5.5 – Reconstruction of a single subscatterer with a dielectric constant of $\varepsilon_r = 3.0 - j\,5.0$.

As shown in the figures, the algorithm calculates the position of the single scatterer accurately; however, the value of the dielectric constant is not calculated accurately. For the real parts of the dielectric, the position of the single scatterer was satisfactorily calculated. The values for the real part of the dielectric constant for the single scatterer as plotted as a function of the loss factor of patch 17 is shown in figure 5.6.

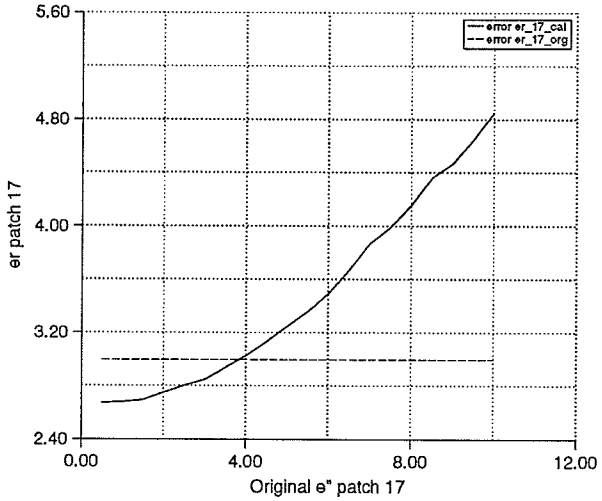

Fig. 5.6 – Real dielectric constant of patch 17 versus loss factor ϵ'' of patch 17.

The graph, figure 5.6, shows the calculated values for the real dielectric constant increasing almost exponentially with the value of the complex part. Using an error constraint of +/– 10% of the original value, acceptable results could be obtained in the range of complex dielectric constant of –j 0.0 to –j 5.5 where the corresponding calculated values for the real dielectric constant were 2.686 and 3.356 respectively. The error constant α_{err} was plotted as a function of the loss factor of patch 17. The results are shown in figure 5.7.

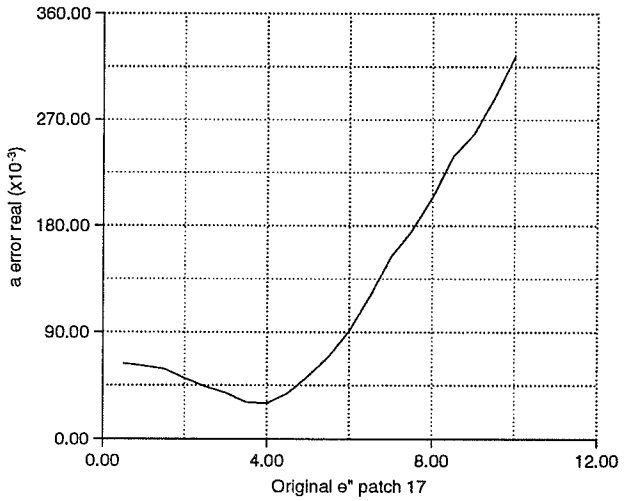

Fig. 5.7 – Real reconstruction error versus loss factor ϵ'' of patch 17.

The graph, figure 5.7, shows a dip in the minimum at a value of –j 4.0 and then grows exponentially. Since the target space is reconstructed with reasonable accuracy, most of the error comes from the calculation of the dielectric constant of the single scatterer. From figure 5.6 it can be seen that the real dielectric constant is calculated correctly for a value of ε'' = –j 4.0 which in turn leads to the minimum value for α_{err} when the complex dielectric constant equals –j 4.0.

The results of the reconstruction for the complex part of the dielectric constant again determined the position of the scatterer, but the complex part of the dielectric constant could not be calculated accurately for the larger values. Figure 5.8 shows a plot of the calculated imaginary dielectric constant ϵ'' as a function of the original imaginary dielectric constant.

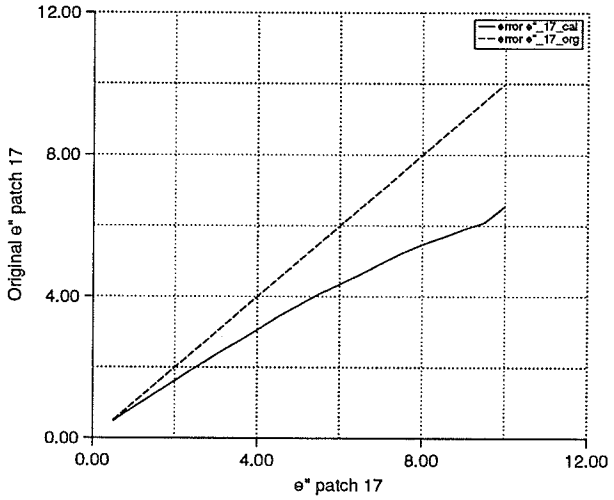

Fig. 5.8 – Calculated loss factor of patch 17 versus original loss factor ϵ'' of patch 17.

The graph, figure 5.8, shows the difference in the calculated values and the original values of the loss factor ϵ'' of patch 17 increasing as the original value increases. Characteristic of the algorithm's ability to calculate the dielectric constant in other circumstances, there is a leveling off of the results. Figure 5.9 shows a graph of the error α_{err} as a function of the loss factor of patch 17.

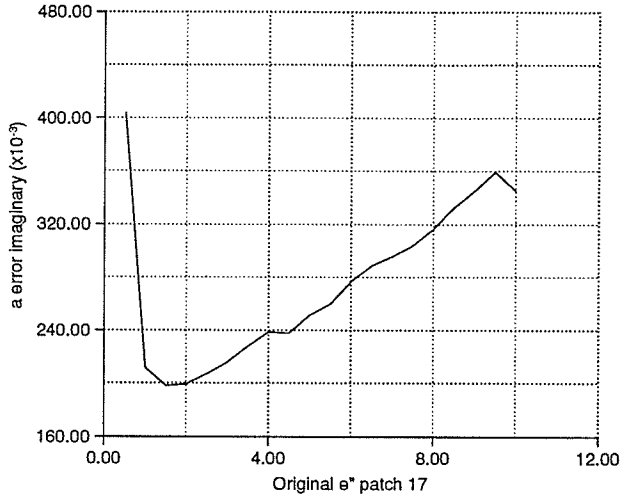

Fig. 5.9 – Loss factor reconstruction error versus loss factor of patch 17.

Figure 5.9 shows a high initial value for α_{err} but then drops to a minimum around $\epsilon'' = -j$ 1.5 before increasing linearly as ϵ'' increases. The high value of α_{err} can be associated with the difficulty involved in calculating the values for ϵ'' which are close to zero. As the original values for ϵ'' increase, the calculated values for ϵ'' in the target region are reasonably accurate, leaving most of the value of α_{err} coming from the calculation of ϵ'' for the single scatterer at position 17. As seen in figure 5.8, the calculated values for ϵ'' for the scatterer fall short of the original values as the original values increase. This in turn explains the increasing values of α_{err} as the original ϵ'' increases.

5.2 Results From a Lossy Dielectric Target Region with a Single Scatterer

For most practical applications of microwave imaging, the target to be reconstructed will have to have both the dielectric properties and the conductive properties taken into account. The loss of the dielectric target poses two problems in the reconstruction. First,

the loss will affect the intrinsic impedance of the cylinder which in turn will affect the amount of microwave energy being coupled into the medium. Secondly, the total electric field in one of the patches could approach numerical zero which would result in a discontinuity of the solution coming from the division carried out in equation (3.27).

A single scatterer at position 17, as done in previous examples, was used to generate the results in this section. The complex dielectric constant of the single scatterer was held constant at $\varepsilon_r^* = 2.0 - j\,0.5$. The real component of the dielectric constant of the target region was held constant a $\varepsilon_r = 1.2$ while the imaginary component was varied from $-j\,0.1$ to $-j\,0.5$. These results are shown in figures 5.10 to 5.14.

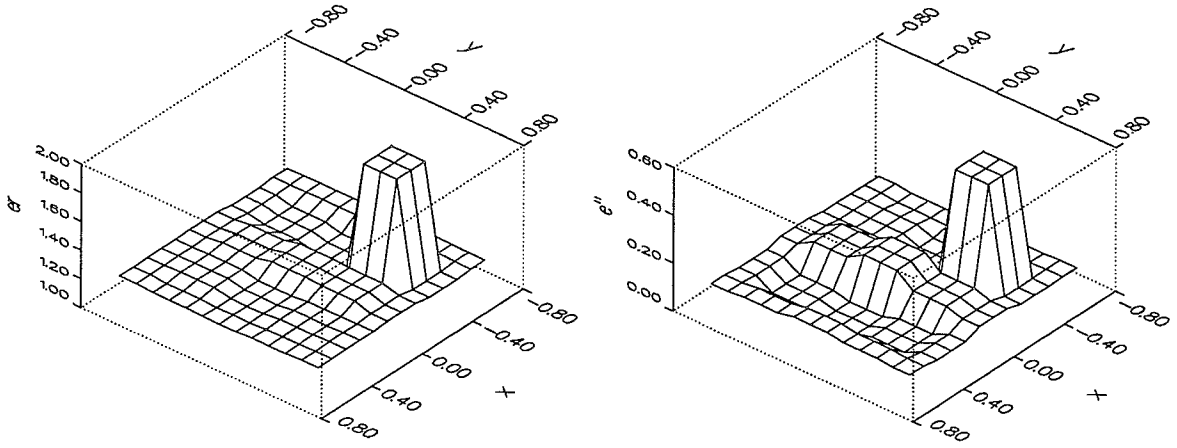

(a) Dielectric reconstruction

(b) Loss factor reconstruction

Fig. 5.10 – Reconstruction of cylinder with a target space dielectric constant of $\varepsilon_r = 1.2 - j\,0.1$.

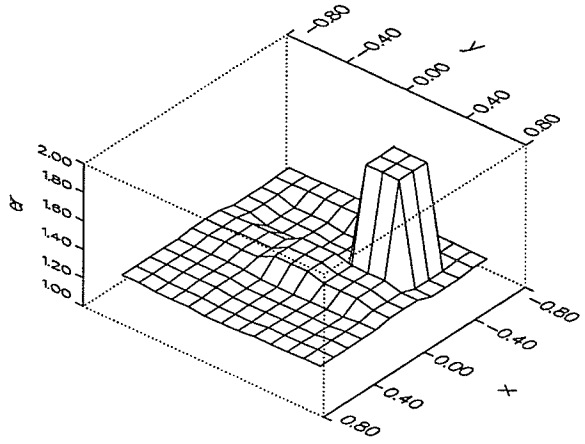

(a) Dielectric reconstruction

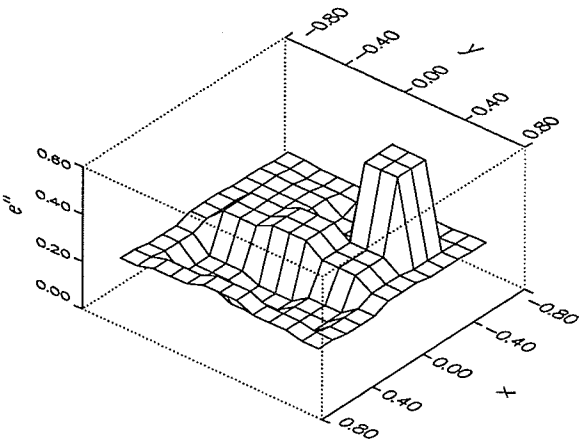

(b) Loss factor reconstruction

Fig. 5.11 – Reconstruction of cylinder with a target space dielectric constant of $\varepsilon_r = 1.2 - j\,0.2$.

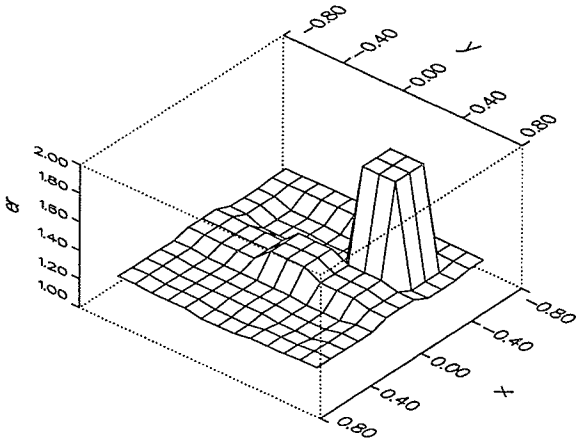

(a) Dielectric reconstruction

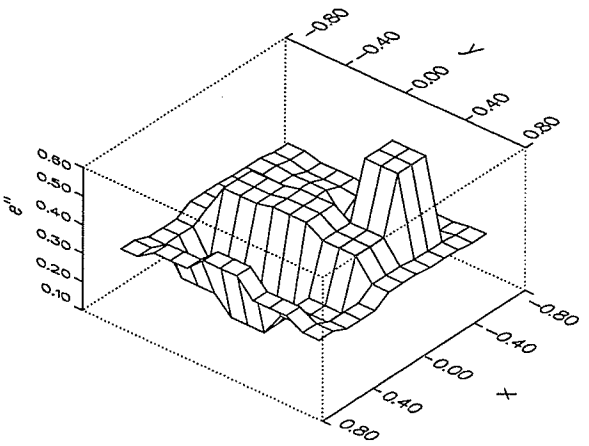

(b) Loss factor reconstruction

Fig. 5.12 – Reconstruction of cylinder with a target space dielectric constant of $\varepsilon_r = 1.2 - j\,0.3$.

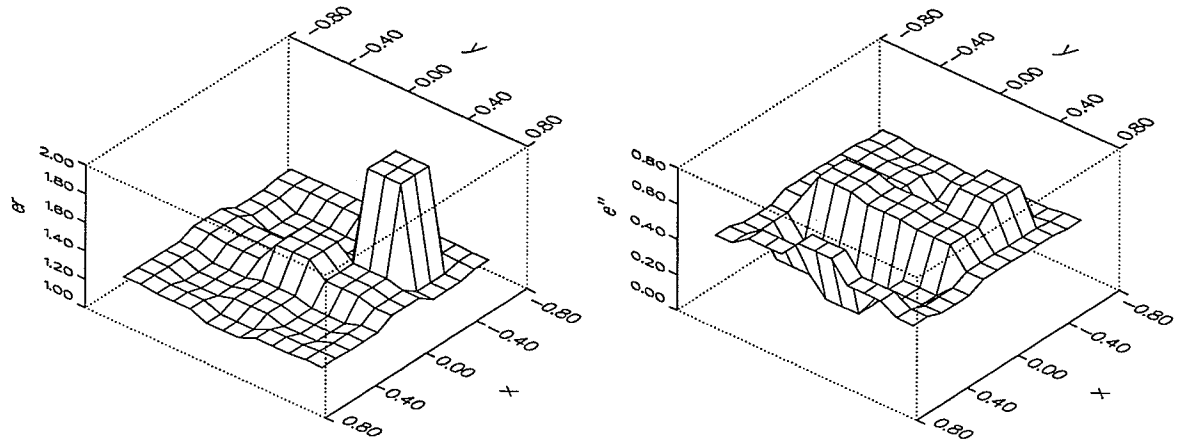

(a) Dielectric reconstruction (b) Loss factor reconstruction

Fig. 5.13 – Reconstruction of cylinder with a target space dielectric constant of $\varepsilon_r = 1.2 - j\,0.4$.

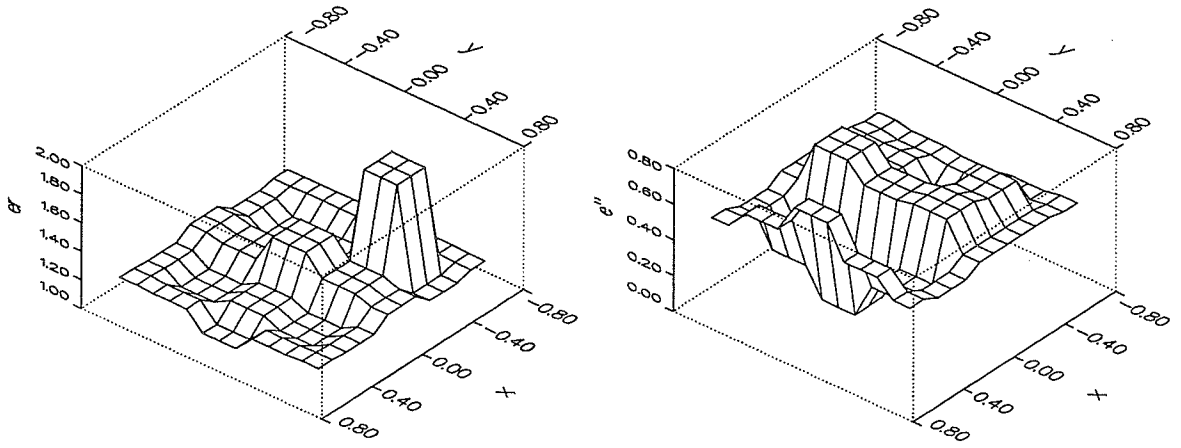

(a) Dielectric reconstruction (b) Loss factor reconstruction

Fig. 5.14 – Reconstruction of cylinder with a target space dielectric constant of $\varepsilon_r = 1.2 - j\,0.5$.

Figures 5.10 to 5.14 show that the dielectric loss of target space has a relatively small effect on the reconstruction of the dielectric permittivity of the cylinders. In all cases the position of the subscatterer is determined, and the value for the dielectric constant for the subscatterer is also determined. The values of the dielectric constant of the subscatterer at

position 17 are graphed as a function of the complex dielectric constant ϵ'' for the target region in figure 5.15. This figure shows reasonably good values of ε_r for patch 17 with all the values staying close to 1.9, but slowly decreasing as the loss factor of the target space is increased. The effect of the loss factor of the target region on the overall reconstruction of the real dielectric cross section also seems relatively low compared to the previous examples shown in subsection 4. 4. 2 . In figures 5.10 (a) to 5.14 (a) the dielectric constant of the target space is approximately 1.2. It is not until the loss factor of the target space is equal to –j 0.5 in figure 5.14 that the dielectric cross section is affected.

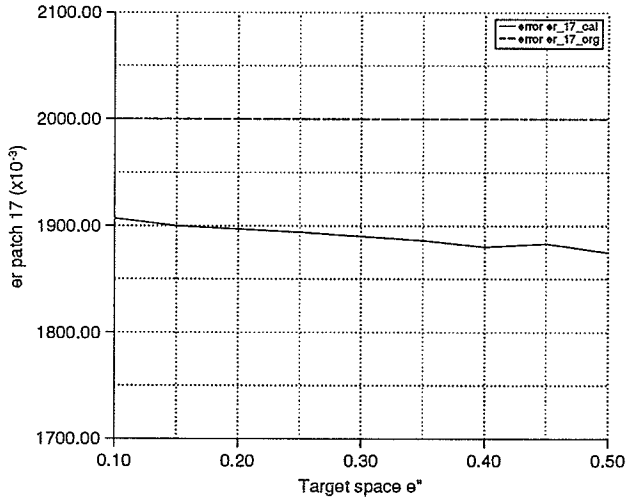

Fig. 5.15 – Dielectric constant of patch 17 versus ϵ'' of the target region.

Figure 5.16 shows the error for the real dielectric cross sections as a function of complex dielectric constant of the target region. As shown in the previous figures, initially the real dielectric cross sections are not affected, but as the loss factor of the target region increases, the accuracy of the resulting reconstructions decreases.

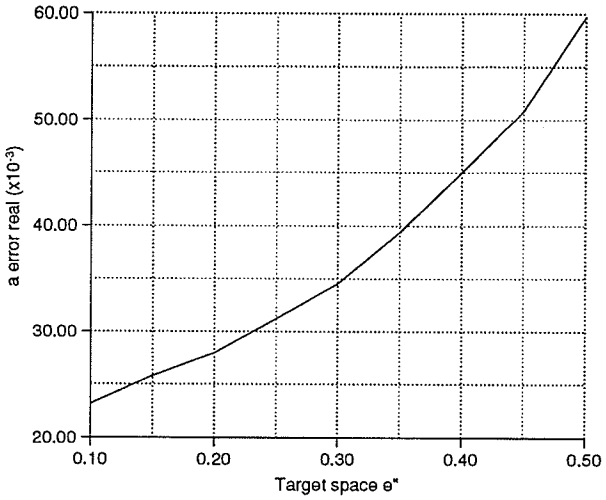

Fig. 5.16 – Error for the real reconstruction versus ϵ'' for the target region.

In the case of the loss factor cross section reconstructions, the loss factor of the original target space has a great effect on the reconstruction. In figures 5.10 (b) to 5.14 (b) reconstructions are steadily degraded with the increasing loss factor of the target region. When the loss has a value of –j 0.4, the position of the subscatterer can no longer be made out. Even for the lower values of the loss factor of the target region, the reconstructed loss factor cross section is corrupted; likewise, when the position of the subscatterer can be made out, it is still difficult to determine the loss factor of the target region. Figure 5.17 shows the values for the loss factor of patch 17 as a function of the loss factor of the target region, and figure 5.18 shows the error for the reconstruction of the loss factor as a function of the loss of the target region. Both figures show a dramatic increase in error for larger values of the target space loss factor. Determining the position of the scatterer seems to be the limiting factor in the usefulness of the reconstructions. If the error criterion was quite high, 20% for example, then according to figure 5.17 acceptable reconstructions can be obtained for values of the target region loss factor of –j 0.375. However, it is evident from figures 5.12 (b) and

5.13 (b) that the reconstructions are limited by the ability to calculate the position of the subscatterer, and from these it is determined that the true limit for the target space loss factor is somewhere between –j 0.175 and –j 0.20.

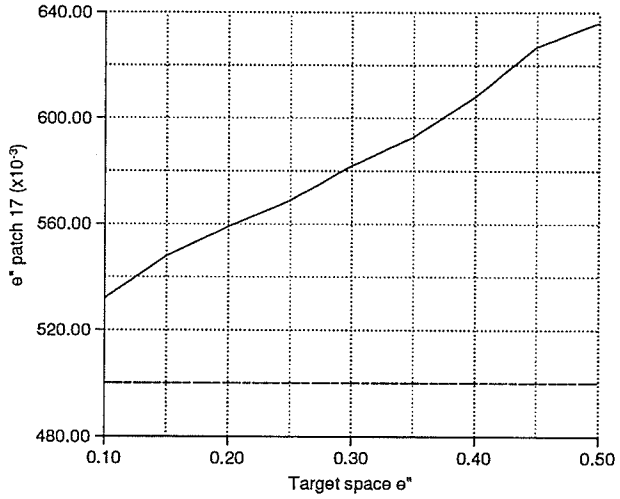

Fig. 5.17 – Loss factor of patch 17 versus loss factor of the target region.

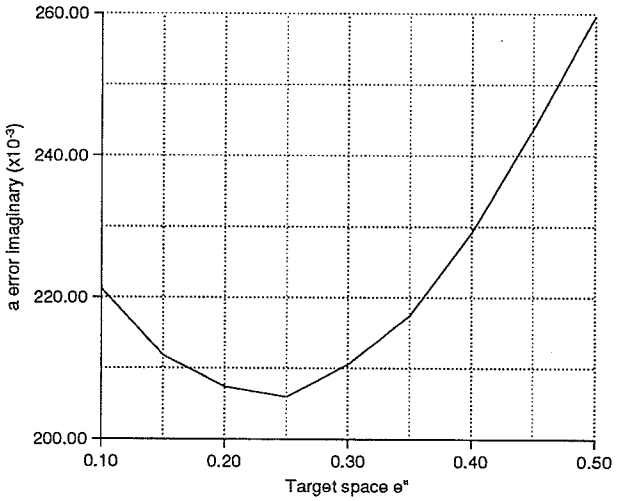

Fig. 5.18 – Reconstruction error versus loss factor of the target region.

Chapter 6 Discussion and Future Work

The algorithm described in Chapter 3 is a very general one which makes as few approximations and assumptions about the target as possible. This general type of algorithm is very flexible which is needed in order to be useful in a broad range of applications. Before finding its way into any practical role, there are many areas that should be investigated. The additional work suggested are two of many areas that could be investigated further.

6. 1 Image Reliability

In all of the example results shown in this thesis, the error constant α_{err} defined by equation (4.1) was used to gauge the reliability of the reconstructed image. However, this equation uses the known dielectric cross section in its calculation which obviously defeats the purpose of using an imaging algorithm in the first place. In some situations there may be other types of information available to confirm the findings of a microwave imaging algorithm. The different types of materials in a target region and their dielectric constants may already be known. The range of dielectric constants could be used to eliminate reconstructions which are grossly erroneous. This does not indicate how good or how bad an image really is. It only indicates whether or not a reconstruction is wrong, but it does not indicate if it is right. Other types of information include knowing the structure of a target. For example, in the case of imaging a human head, the structure is already known and the sight of an anomaly could be known from a CAT scan or NMR image. The position of the skull and other landmarks could then be used to confirm the microwave reconstruction. Again, this does not guarantee that the calculation of the dielectric cross section is correct

because the results shown in subsections 4.4.1 and 4.4.2 show the position of an anomaly calculated with reasonable accuracy; whereas the dielectric constant is not.

There are some indicators in this algorithm which may be used to give a better idea of the reconstruction quality, especially when no previous information about the target is known. One of these could be the condition of the matrix **M**. The program used didn't have the capability to calculate the condition of matrix **M** for any of the cases studied, but it is one area that could use some investigation. The number of iterations used to invert the matrix **M** was investigated with the expectation that more iterations would be required to obtain a solution for matrix equations which had a higher condition number. No correlation was found. Another parameter which could give an idea about the status of an image is the normalized error vector coming from the solution of equation (3.21). This vector is defined as the vector norm of the difference between the sampled scattered field and the calculated scattered field and is obtained by multiplying matrix **M** with the calculated polarization current obtained in equation (3.21).

$$err_{norm} = \| E_{scat}^{sampled} - E_{scat}^{calculated} \| \tag{6.1}$$

where

$$E_{scat}^{calculated} = [\mathbf{M}]\ J_s \tag{6.2}$$

For example, the vector norm for the error of each result in section 5.2 was plotted in figure 6.1 .

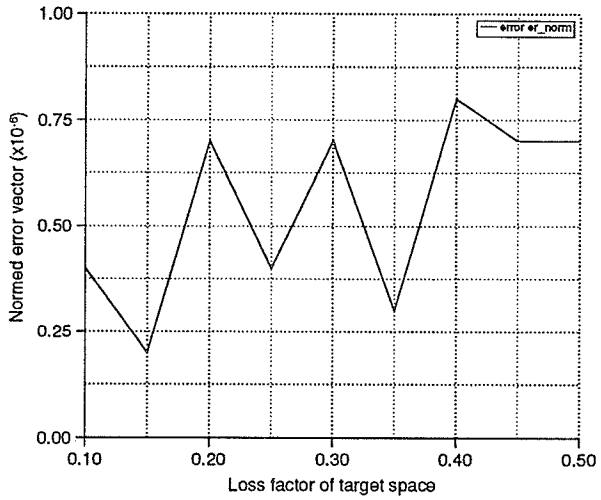

Fig. 6.1 – Vector norm of the error vector versus dielectric loss factor of the target region.

The results do show a general oscillating increase in the vector norm of the error vector which corresponds to the decrease in accuracy observed in the reconstructions shown in section 5.2 , and thus do show some promise as an indication of the accuracy of the reconstruction. Unfortunately, the plot of the error vector in the example reconstructions in subsection 4.4.2 showed no correlation between the error vector and the accuracy of the reconstructions.

6. 2 Target Approximations and Algorithm Formulations for Image Enhancement

The general algorithm presented here was written to be flexible enough to handle most applications. There are some cases where some flexibility can be exchanged for better reconstruction performance. The method proposed is one that takes advantage of the symmetry of the target. In the case of asymmetric imaging, the target is assumed to be symmetrical, and the algorithm is rewritten to reconstruct the anomalies which are asymmetric.

6. 2. 1 Asymmetric Imaging Algorithm

In some applications the symmetry of the target can be taken advantage of in order to improve upon the performance of the algorithm. There are many examples of symmetric targets where such an approach could be used. For the most part the human body is symmetric, except for the internal organs of the middle thorax, such as the liver and the stomach. However, the upper chest, and the lower abdominal areas are symmetric to a fair degree, and the head and neck are totally symmetric. In this formulation there is only a single asymmetric scatterer, and the side it is taken to be known.

The algorithm is based upon the superposition of two target regions. One being the symmetric component and the other being the asymmetric component as shown in figure 6.2 .

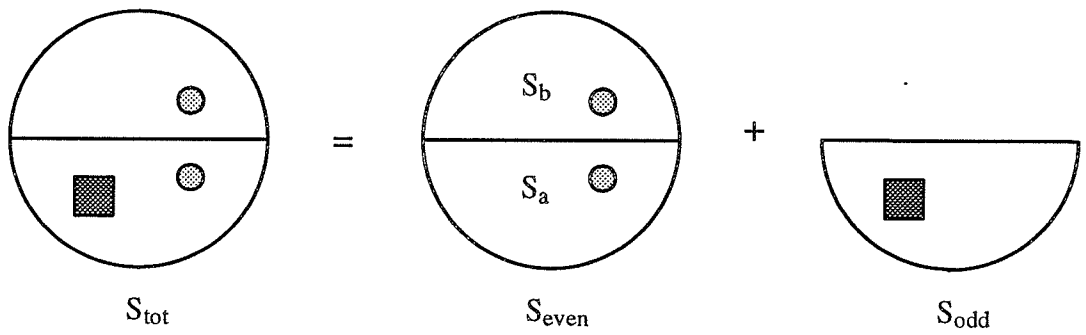

Fig. 6.2 – Superpostion of target spaces.

As shown in the figure, the contrast S_{tot} is made up of the addition of the contrast S_{even} and S_{odd}. The symmetric target space S_{even} is further divided into upper half, S_b, and a lower half S_a. The setup used to measure the scattered field is shown in figure 6.3 .

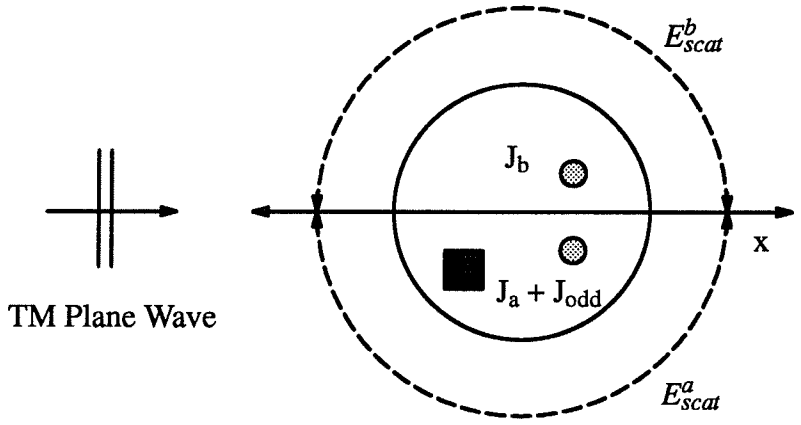

Fig. 6.3 – Measurement setup.

The cylinder is illuminated with a TM plane wave incident from the negative x direction so that it is symmetric about the x axis.

The formulation is based upon the fact that the difference in the scattered fields E^a_{scat} and E^b_{scat} will be caused by the square asymmetry. On the cylinder three polarizations currents are defined. These are J_b for the upper symmetric half cylinder, J_a for the lower symmetric cylinder, and J_{odd} for the asymmetric lower cylinder. Assuming that the asymmetry only affects E^a_{scat}, then this scattered field can be calculated from the polarization current J_a and J_b as follows:

$$E^b_{scat} = \int_{Sa} J_a \, G(k\varrho) ds_a + \int_{Sb} J_b \, G(k\varrho) ds_b \tag{6.3}$$

where S_a and S_b are the upper and lower halves of the symmetric target space S_{even}. The scattered field is then written in terms of J_a, J_b, and J_{odd} as follows:

$$E^a_{scat} = \int_{Sa} J_a \; G(k\varrho) ds_a + \int_{Sb} J_b \; G(k\varrho) ds_b + \int_{Sa} J_{odd} \; G(k\varrho) ds_a \tag{6.4}$$

It is assumed that the asymmetry in the lower target region does not affect the scattered field E^b_{scat} for the upper target region. The higher the average loss factor of the symmetric region is, the more valid this assumption becomes. This is because the field produced by a current on the asymmetric patch is attenuated as it passes through the symmetric region and out to where the scattered field E^b_{scat} is sampled. Using this assumption, allows one to use the information in the scattered field E^b_{scat} to calculate the symmetric polarization current distributions J_a and J_b. Using the steps outlined in Chapter 3, the integral equation (6.3) can be transformed into the following matrix equation:

$$E^b_{scat} = [\mathbb{G}^a] \; J_a + [\mathbb{G}^b] \; J_b \tag{6.5}$$

Since $J_a(x,y)$ and $J_b(x,y)$ are the polarization currents for the symmetric target areas, it follows that they should also be symmetric, and hence $J_a(x,y) = J_b(x,-y)$. Using this fact in equation (6.5) gives the following which only has to be solved for half of the symmetric polarization current.

$$E^b_{scat} = [\mathbb{G}^a] \; J_b + [\mathbb{G}^b] \; J_b \tag{6.6}$$

$$E^b_{scat} = \{[\mathbb{G}^a] + [\mathbb{G}^b]\} \; J_b \tag{6.7}$$

Equation (6.7) is then solved for J_b using the conjugate gradient method described in appendix A. It is in this step where the benefit of the assumptions is made. The benefit is that the size of the matrix being inverted, the summation of matrices $\mathbf{G}^a$ and $\mathbf{G}^b$, is half the size of the corresponding matrix **M** in the general formulation in Chapter 3.

$$\{[\mathbf{G}^a] + [\mathbf{G}^b]\}^{-1} E^b_{scat} = J_b \tag{6.8}$$

Equation (6.4) is used to determine the asymmetric polarization current J_{odd}. In equation (6.4) the summation of the first two integrals make up the symmetric component of the scattered field E^a_{scat} and is equal to E^b_{scat} with the sign on the y component reversed.

$$E^a_{scat}(x,y) = \underbrace{\int_{Sa} J_a\, G(k\varrho)ds_a + \int_{Sb} J_b\, G(k\varrho)ds_b}_{E^b_{scat}\ (x,-y)} + \int_{Sa} J_{odd}\, G(k\varrho)ds_a \tag{6.9}$$

$$E^a_{scat}(x,y) = E^b_{scat}(x,-y) + \int_{Sa} J_{odd}\, G(k\varrho)ds_a \tag{6.10}$$

$$E^a_{scat}(x,y) - E^b_{scat}(x,-y) = \int_{Sa} J_{odd}\, G(k\varrho)ds_a \tag{6.11}$$

The integral equation (6.11) is then transformed into a matrix equation by the same methods used in Chapter 3 to give the following:

$$E^a_{scat}(x,y) - E^b_{scat}(x,-y) = [\mathbf{G}^a]\, J_{odd} \tag{6.12}$$

Using the conjugate gradient method as done previously, equation (6.12) is then solved for the asymmetric polarization current J_{odd}.

$$[\mathbf{G}^a]^{-1}\{E^a_{scat}(x,y) - E^b_{scat}(x,-y)\} = J_{odd} \tag{6.13}$$

Once the polarization currents J_a, J_b, and J_{odd} are obtained, then the total electric field is calculated so that the contrast vector S_{odd} and S_{even} can be calculated. . To calculate the contrast vector S_{even}, the total electric field representing the even component of the scattered field is calculated as follows:

$$E^{int}_{scat}(x,y) = \int_{Sa} J_a \; G(k\varrho)ds_a + \int_{Sb} J_b \; G(k\varrho)ds_b \tag{6.14}$$

Since the internal scattered field for the even component is symmetric, the internal scattered field $E^{int}_{scat}(x,y)$ only has to be calculated for the upper or lower half of the cylinder. Adding the incident field to the internal scattered field gives the total field.

$$E^{even}_{tot} = E^{int}_{scat} + E^{even}_{inc} \tag{6.15}$$

Finally, the contrast vector S_{even} can be calculated from the total even electric field E^{even}_{tot} and the even polarization current J_{even} as follows:

$$S_{even} = \frac{J_{even}}{E^{even}_{tot}} \tag{6.16}$$

The total electric field for the odd component of the scattered field is calculated by integrating all three of the polarization currents and the corresponding Green's function over the target regions.

$$E^{int}_{scat}(x,y) = \int_{Sa} J_a \; G(k\varrho)ds_a + \int_{Sb} J_b \; G(k\varrho)ds_b + \int_{Sa} J_{odd} \; G(k\varrho)ds_a \tag{6.17}$$

Equation (6.17) is used to calculate the internal scattered field for points in the upper region and in the lower region. To get the total scattered field, the incident field is added to the internal scattered field.

$$\begin{aligned} E^a_{tot} &= E^{a\,int}_{scat} + E^a_{inc} \\ E^b_{tot} &= E^{b\,int}_{scat} + E^b_{inc} \end{aligned} \tag{6.18}$$

To calculate the odd total electric field, E^b_{tot} is reflected and is subtracted from E^a_{tot} to yield E^{odd}_{tot}.

$$E^{odd}_{tot} = E^a_{tot} - E^b_{tot} = E^{aint}_{scat} + E^a_{inc} - E^{bint}_{scat} - E^b_{inc} \tag{6.19}$$

Since the refection of the incident field E^a_{inc} is equal to the incident field E^a_{inc}, equation (6.19) is reduced to the following:

$$E^{odd}_{tot} = E^a_{tot} - E^b_{tot} \tag{6.20}$$

From the total odd electric field E^{odd}_{tot}, the contrast vector S_{odd} is found by dividing each element in the vectors.

$$S_{odd} = \frac{J_{odd}}{E^{odd}_{tot}} \tag{6.21}$$

Finally, from the two contrast vectors S_{even} and S_{odd}, the dielectric properties can be calculated as shown below.

$$\epsilon_{ri}^{even} = \mathrm{Re}\left\{\frac{S_{eveni}}{k_o^2} + 1\right\}$$
$$\epsilon_{i}^{''even} = \mathrm{Im}\left\{\frac{S_{eveni}}{k_o^2}\right\} = \frac{\sigma_{even}}{\omega \epsilon_o} \tag{6.22}$$

$$\epsilon_{ri}^{odd} = \mathrm{Re}\left\{\frac{S_{oddi}}{k_o^2} + 1\right\}$$
$$\epsilon_{i}^{''odd} = \mathrm{Im}\left\{\frac{S_{oddi}}{k_o^2}\right\} = \frac{\sigma_{odd}}{\omega \epsilon_o} \tag{6.23}$$

6. 2. 2 Asymmetric Imaging Algorithm Discussion

Overall the asymmetric imaging algorithm performed poorly. The only success came when imaging lossy cylinders which were slightly asymmetric, that being a single asymmetric anomaly with a dielectric constant 5% higher than the symmetric target region. Even in these cases the reconstruction of the odd target region was dismal and the reconstruction of the even target region was not always reliable. The reasons for the poor results are unknown. The problems may lie in the formulation itself or perhaps in the implementation. There are areas in the algorithm which could be changed, such as the definition of E_{tot}^{odd}. A suggested change would be to define E_{tot}^{odd} as the integration over the odd polarization component J_{odd} only. Another variation would be to use a complete odd target space instead of the half target space which was used.

The failure of this algorithm should not put to rest the investigation into asymmetric imaging algorithms. It is the belief of the author that the symmetry of a target could be used to increase the performance of a microwave imaging algorithm and that such an algorithm would have many applications.

Chapter 7 Conclusions

This thesis presented a microwave imaging algorithm based on an inverse scattering approach. The performance of the algorithm was demonstrated using a computer program to generate the reconstructions of both lossless and lossy inhomogenious dielectric cylinders. Some selected characteristics of the cylinders were changed to determine what effect they would have on the algorithm's ability to generate a reconstruction.

The first set of results were generated from lossless cylinders. A previously published result for a lossless cylinder was reproduced to validate the algorithm. Various parameters of target cylinders were then changed to judge the versatility of the algorithm. These parameters were the position of a single scatterer in a free space target region, the number of total patches in a target region, the number of free space patches in a target region, dielectric variations in a single scatterer, and variations of the target region dielectric constant with a single scatterer present. In almost all of the cases the accuracy of the imaging algorithm was limited by its ability to calculate the dielectric constant. The only exception was in the case where the dielectric constant of the target region was varied. In this case the reconstruction was limited by the ability of the algorithm to determine the position. The drastic effect that the dielectric constant of the target region had on the ability to reconstruct the dielectric cross section was thought to have been caused by the wave compression of the high dielectric over a larger area.

The most general target studied in this work was a lossy inhomogenious dielectric cylinder. The performance of the algorithm was investigated using two types of test targets.

One being a single lossy target cylinder in a free space target region and the other being a lossy cylinder with a single anomaly. In the case of the single scatterer, the reliability of the algorithm was limited by the calculation of the dielectric properties of the target. The position of the target was determined accurately in both the dielectric and loss factor reconstructions. For the case of the single scatterer in a lossy target region, the performance of the dielectric constant reconstructions was limited by the ability of the algorithm to calculate the dielectric constant of the anomaly. On the other hand, the loss factor reconstructions were limited by the ability of the algorithm to determine the position of the anomaly and its corresponding loss factor.

The asymmetric imaging algorithm presented had some limited success in reconstructing the even component of a slightly asymmetric target. No consistent results were obtained. It is the belief of the author that some more work in this area would result in a useful algorithm.

References

[1] L. E. Larsen and J. H. Jacobi, *Medical Applications of Microwave Imaging*, IEEE Press, New York, 1986.

[2] C. C. Johnson and A. W. Guy, "Nonionizing Electromagnetic Wave Effects in Biological Materials and Systems," Proc. IEEE, vol. 60, pp. 692–718, 1972.

[3] D. E. Livesay and K. M. Chen, "Electromagnetic Fields Induced Inside Arbitrary Shaped Biological Bodies," IEEE Trans. Microwave Theory Tech., vol. MTT–22, pp. 1273–1280, 1974.

[4] J. C. Lin and M. J. Clarke, "Microwave Imaging of Cerebral Edema," Proc. IEEE, vol. 70, pp. 523–524, 1982.

[5] L. E. Larsen and J. H. Jacobi, "Microwave Scattering Parameter Imagery of an Isolated Canine Kidney," Med. Phys., vol. 5, pp. 394–403, 1979.

[6] L. E. Larsen and J. H. Jacobi, "Microwave Time Delay Spectroscopic Imagery of Isolated Canine Kidney," Med. Pys., vol.7, pp. 1–7, 1980.

[7] M. F. Iskander, R. Maini, C. H. Durney, and D. G. Bragg, "A Microwave Method for Measuring Changes in Lung Water," IEEE Trans. Biomed. Eng., vol. BME–28, N12, pp. 797–804, 1981.

[8] D. A. Christensen and C. H. Durney, "Hyperthermia Production for Cancer Therapy, a Review of Fundamentals and Methods," J. Microwave Power, vol. 16, pp. 89–105, 1981.

[9] P. C. Meyers, N. L. Sadowsky, and A. H. Barrett, "Microwave Thermography Principals, Methods, and Clinical Applications," J. Microwave Power, Vol. 14, pp. 105–115, 1979.

[10] D. D. N'Guyen, A. Mamouni, Y. Leroy, and I. Constant, "Simultaneous Microwave Local Heating and Microwave Thermography Possible Clinical Applications," J. Microwave Power, vol. 14, pp 135–138, 1979.

[11] C. Pichot, L. Jofre, G. Peronnet, and J.–C. Bolomey, "Active Microwave Imaging of Inhomogeneous Bodies," IEEE Trans. Anten. Prop., vol. AP–33, pp. 416–425, 1985.

[12] J. Bolomey, A. Izadnegahdar, L. Jofre, C. Pichot, G. Peronnet, and M Solaimani, "Microwave Diffraction Tomography for Biomedical Applications," IEEE Trans. Microwave Theory Tech., vol. MTT–30, pp. 1998–2000, 1982.

[13] J. C. Lin, "Frequency Optimization for Microwave Imaging of Biological Tissues," Proc. IEEE, vol. 73, pp. 374–375, 1985.

[14] J. H. Jacobi, L. E. Larsen, and C. T. Hast, "Water–immersed Microwave Antennas and Their Application to Microwave Interrogation of Biological Target," IEEE Trans. Microwave Theory Tech., vol. MTT–27, pp. 70–78, 1979.

[15] R. Brooks, and G. Dichiro, "Principles of Computer Assisted Tomography (CAT) in Radiographic and Radioisotropic Imaging," Phys. Med. Biol., vol. 21, pp. 689–732, 1976.

[16] H. Ermert, G. Fulle, and D. Hiller, "Microwave Computerized Tomography," in Proc. XIth European Microwave Conf., pp. 421–425, 1981.

[17] R. Maini, M. F. Iskander, C. H. Durney, and M. Berggren, "On the Sensitivity and the Resolution of Microwave Imaging Using ART," Proc. IEEE, vol. 69, pp 1517–1519, 1981.

[18] M. Tasto and H. Schomberg, "Object reconstruction from projections and some nonlinear extensions," presented at NATO Advanced Study Institute on Pattern Recognition and Signal Processing, Paris, France, June 25–July 4, 1979.

[19] J. H. Jacobi and L. E. Larsen, "Microwave Interrogation of Dielectric Targets. Part II: By Microwave Time Delay Spectroscopy," Med. Phys., vol. 5, pp. 509–513, 1978.

[20] R. F. Harrington, *Field Computation by Moment Methods*. New York: Macmillan, 1968.

[21] M. M. Ney, A. M. Smith, and S. S. Stuchly, "A Solution of Electromagnetic Imaging Using PseudoInverse Transformation," IEEE Trans. Med. Imaging, vol. MI–3, pp. 155–162, 1984.

[22] L. Garnero, A. Franchois, J.–P. Hugonin, C. Pichot, and N. Joachimowicz, "Microwave Imaging – Complex Permittivity Reconstruction by Simulated Annealing," IEEE Trans. Microwave Theory Tech., vol. MTT–39, pp 1801–1807, 1991.

[23] N. Joachimowicz, C. Pichot, and J.–P. Hugonin, "Inverse Scattering: An Iterative Numerical Method for Electromagnetic Imaging," IEEE Trans. Anten. Prop., vol. AP–39, pp. 1742–1752, 1991.

[24] S. Caorsi, G. Gragnani, and M. Pastorino, "Two–Dimensional Microwave Imaging by a Numerical Inverse Scattering Solution," IEEE Trans. Microwave Theory Tech., vol. MTT–38, pp. 981–988, 1990.

[25] M. M. Ney, "Method of Moments as Applied to Electromagnetic Problems," IEEE Trans. Microwave Theory Tech., vol. MTT–33, pp. 972–980, 1985.

[26] J. Richmond, "Scattering by a Dielectric Cylinder of Arbitrary Cross Section Shape," IEEE Trans. Anten. Prop., vol. AP–13, pp. 334–341, 1965.

[27] D. K. Ghodgaonkar, O. P. Gandhi, and M. J. Hagmann, "Estimation of Complex Permittivities of Three–Dimensional Inhomogeneous Biological Bodies," IEEE Trans. Microwave Theory Tech., vol. MTT–31, pp. 442–446, 1983.

[28] E. C. Jordan, and K. G. Balmain, *Electromagnetic Waves and Radiating Systems*. Englewood Cliffs, New Jersey, 1968.

APPENDIX A – Formulation for the Conjugate Gradient Method

Beginning with the following matrix equation

$$[\mathbf{M}]\ x = y \tag{A.1}$$

The first step is to generate the first residual error vector r_o using an initial guess x_o.

$$r_o = [\mathbf{M}]\ x_o - y \tag{A.2}$$

The next step is to generate the direction vector d_o.

$$d_0 = -[\mathbf{M}]^H\ r_o \tag{A.3}$$

Where $[\mathbf{M}]^H$ is the transposed complex conjugate of the matrix [M], the successive iterative steps are as follows:

$$x_{n+1} = x_n + t_n\ d_n \tag{A.4}$$

where

$$t_n = \frac{\| [\mathbf{M}]^H\ r_n \|^2}{\| [\mathbf{M}]\ d_n \|^2} \tag{A.5}$$

and

$$r_{n+1} = r_n + t_n[\mathbf{M}]\ d_n \tag{A.6}$$

$$d_{n+1} = [\mathbf{M}]^H\ r_{n+1} + q_n\ d_n \tag{A.7}$$

where

$$q_n = \frac{\| [\mathbf{M}]^H \, r_{n+1} \|^2}{\| [\mathbf{M}]^H \, r_n \|^2} \tag{A.8}$$